

# Precession-induced nonclassicality of the free induction decay of NV centers by a dynamical polarized nuclear spin bath

Mu-Che Lin<sup>1</sup>, Ping-Yuan Lo<sup>2</sup>, Franco Nori<sup>3,4</sup>, and Hong-Bin Chen<sup>1,5,\*</sup>

<sup>1</sup>Department of Engineering Science, National Cheng Kung University, Tainan 701401, Taiwan

<sup>2</sup>Department of Electrophysics, National Yang Ming Chiao Tung University, Hsinchu 300093, Taiwan

<sup>3</sup>Quantum Computing Center, and Theoretical Quantum Physics Laboratory, Cluster for Pioneering Research, RIKEN, Wakoshi, Saitama 351-0198, Japan

<sup>4</sup>Physics Department, University of Michigan, Ann Arbor, MI 48109-1040, USA

<sup>5</sup>Center for Quantum Frontiers of Research & Technology, NCKU, Tainan 701401, Taiwan

\*hongbinchen@gs.ncku.edu.tw

## ABSTRACT

The ongoing exploration of the ambiguous boundary between the quantum and the classical worlds has spurred substantial developments in quantum science and technology. Recently, the nonclassicality of dynamical processes has been proposed from a quantum-information-theoretic perspective, in terms of witnessing nonclassical correlations with Hamiltonian ensemble simulations. To acquire insights into the quantum-dynamical mechanism of the process nonclassicality, here we propose to investigate the nonclassicality of the electron spin free-induction-decay process associated with an NV<sup>-</sup> center. By controlling the nuclear spin precession dynamics via an external magnetic field and nuclear spin polarization, it is possible to manipulate the dynamical behavior of the electron spin, showing a transition between classicality and nonclassicality. We propose an explanation of the classicality-nonclassicality transition in terms of the nuclear spin precession axis orientation and dynamics. We have also performed a series of numerical simulations supporting our findings. Consequently, we can attribute the nonclassical trait of the electron spin dynamics to the behavior of nuclear spin precession dynamics.

Keywords: Hamiltonian ensemble, nonclassicality, NV center, free induction decay, dynamical nuclear spin polarization, nuclear spin precession

## 1 Introduction

Along with the development of quantum theory, the ongoing exploration of the ambiguous boundary between the quantum and the classical worlds has attracted extensive interest<sup>1-4</sup>. Although the intuitive viewpoints, e.g., local realism or commutativity of conjugated observables, are seemingly natural and valid in the classical world, they may result in contradicting predictions in the quantum realm. Therefore, the failure of classical strategies attempting to explain an experimental outcome can be conceived as a convincing evidence of quantum nature beyond classical intuition, or nonclassicality.

One of the most famous paradigms is the experimental violation<sup>5-8</sup> of Bell's inequality<sup>9</sup>, which is derived under the assumptions of realism and locality. With the explicit violation of Bell's inequality, the bipartite correlation demonstrates a genuinely nonclassical nature, i.e., Bell nonlocality<sup>10</sup>, which can never be explained classically in terms of the local hidden variable model. Following the same logic, the nonclassicality of a bosonic field is characterized by the Wigner function<sup>11</sup> or the Glauber-Sudarshan  $P$

representation<sup>12–17</sup>. The negativity in these functions demonstrates nonclassicality with a phase space description.

Additionally, there is another emerging type of nonclassicality considering the nature of quantum dynamical processes. Considerable efforts have been devoted to approaching this problem<sup>18–24</sup>. Noteworthy, these approaches focus on certain nonclassical properties of interest of the quantum systems and continuously monitor their temporal evolutions as indicators of dynamical process nonclassicality. Recently, it has been proposed<sup>25–27</sup> an alternative definition of dynamical process nonclassicality, based on the failure of the classical strategy to simulate the incoherent dynamical process. The classical strategy is formulated in terms of a Hamiltonian ensemble (HE)<sup>28,29</sup>, which was initially devoted to investigating the decoherence induced by a disordered medium or classical noise<sup>30–33</sup>. The classicality behind the HE would become clear after looking for additional insights into the cause of the incoherent dynamics.

Quantum systems inevitably interact with their surrounding environments<sup>34–37</sup>; meanwhile, complicated correlations will be established between the systems and their environments during these interactions. These correlations are typically fragile and transient, as the quantum systems are subject to the fluctuations caused by a huge number of environmental degrees of freedom. As a result, the vanishing of the correlations constitutes one of the main sources of decoherence, leading to incoherent dynamical processes. Therefore, a natural way to classify decoherence is based on the properties of the correlations established during the interactions. However, such a naive classification is not feasible due to the huge number of environmental degrees of freedom, rendering the environments, as well as the established correlations, inaccessible.

On the other hand, it has been shown that the classically correlated system-environment correlation results in an incoherent dynamics admitting HE simulations<sup>25</sup>. This implies that the failure of HE simulations serves as a witness for the establishment of nonclassical correlations during the interactions. Such incoherent dynamics violating HE simulations necessarily appeals to nonclassical correlations, rather than reproduced classically by statistical noise. We therefore proposed to classify an incoherent dynamical process according to the possibility to simulate the reduced system dynamics with HEs. It should be stressed that, in this definition, the actual system-environment correlations are deliberately ignored as they are inaccessible to the reduced system exclusively; meanwhile, we attempt to reproduce the incoherent effects on the reduced system classically by using HE simulations.

Additionally, this HE-simulation approach can be further promoted to a representation of the incoherent dynamics over the frequency domain, referred to as the canonical Hamiltonian ensemble representation (CHER)<sup>26</sup>. This is reminiscent of the conventional Fourier transform, transforming a temporal sequence into its frequency spectrum. In contrast, CHER is defined in accordance with the underlying algebraic structure of the HE, highlighting its difference from the conventional one by the non-Abelian algebraic structure<sup>29</sup>. Along with the quasi-distribution of the CHER, we can define a quantitative measure of nonclassicality<sup>26</sup>. Moreover, we place particular emphasis on the practical viability, as this approach relies only on the information of the reduced system, irrespective of the inaccessible environment.

Although dynamical process nonclassicality has been investigated from a quantum-information-theoretic perspective, its quantum-dynamical mechanism is still not understood. To acquire insights into the system-environment interactions giving rise to the classicality-nonclassicality transition, meanwhile underpinning the practical viability of this approach, we will discuss the CHER of the free-induction-decay (FID) process of the electron spin associated with a single negatively charged nitrogen-vacancy (NV<sup>-</sup>) center in diamond. Due to its unique properties, particularly its long coherence time even at room temperature<sup>38–42</sup>, NV<sup>-</sup> centers are a promising candidate for applications in various branches of quantum technologies, ranging from quantum information processing<sup>42–47</sup>, highly-sensitive nanoscale magnetometry<sup>48,49</sup> and electrometry<sup>50,51</sup>, bio-sensing in living cells<sup>52,53</sup>, emerging quantum materials<sup>54–56</sup>, to test

bed of fundamental quantum physics<sup>57</sup>. The primary source of decoherence of the electron spin comes from the hyperfine interaction to the nuclear spin bath of carbon isotopes <sup>13</sup>C randomly distributed in the diamond lattice. Therefore, several techniques have been developed for prolonging the coherence time by engineering the nuclear spin bath, including the isotopic purification<sup>40-42</sup> and dynamic nuclear spin polarization (DNP)<sup>58,59</sup>.

Here we investigate how the nonclassicality of the FID process is induced by the nuclear spin precession dynamics. Since the external magnetic field and the nuclear spin polarization are two experimentally controllable mechanisms manipulating the nuclear spin precession dynamics, we found that the dynamical behavior of FID and the corresponding CHER are sensitive to both controllable properties. We have also observed a transition between classicality and nonclassicality by engineering the nuclear spin bath via the polarization orientation, particularly the  $x$  component of the polarization. Consequently, we can attribute the nonclassical traits of the electron spin FID process to the behavior of nuclear spin precession dynamics based on the response to two controllable properties. Finally, in order to underpin the experimental viability of our numerical simulation, we also present an experimental pulse sequence for carrying out the model.

## 2 Theory of dynamical process nonclassicality

### 2.1 Decoherence under Hamiltonian ensembles

The central role in our approach, modeling an incoherent dynamics, is played by the Hamiltonian ensemble (HE)  $\{(p_\lambda, \hat{H}_\lambda)\}_\lambda$ , which consists of a collection of traceless Hermitian operators  $\hat{H}_\lambda \in \mathfrak{su}(n)$  associated with a probability  $p_\lambda$  of occurrence [figure 1(a)]. The index  $\lambda$  could be very general and may be continuous and/or a multi-index. Every member Hamiltonian operator  $\hat{H}_\lambda$  acts on the same system Hilbert space, leading to a unitary time-evolution operator  $\hat{U}_\lambda(t) = \exp(-i\hat{H}_\lambda t)$ . Then a HE will randomly assign an initial state  $\rho(0)$  to a certain unitary channel  $\hat{U}_\lambda(t)$  according to  $p_\lambda$ , giving rise to an ensemble-averaged dynamics described by

$$\bar{\rho}(t) = \mathcal{E}_t\{\rho(0)\} = \int p_\lambda \hat{U}_\lambda(t) \rho(0) \hat{U}_\lambda^\dagger(t) d\lambda. \quad (1)$$

Irrespective of the unitarity of each single channel, the ensemble-averaged dynamics (1) demonstrates an incoherent behavior due to the averaging procedure over all unitary realizations<sup>28-30</sup>. For instance, when a single qubit is subject to spectral disorder with a HE given by  $\{(p(\omega), \omega\hat{\sigma}_z/2)\}_\omega$ , where  $p(\omega)$  can be any probability distribution function [figure 1(b)], it undergoes a pure dephasing dynamics given by

$$\bar{\rho}(t) = \int_{-\infty}^{\infty} p(\omega) e^{-i\omega\hat{\sigma}_z t/2} \rho_0 e^{i\omega\hat{\sigma}_z t/2} d\omega = \begin{bmatrix} \rho_{\uparrow\uparrow} & \rho_{\uparrow\downarrow} \phi(t) \\ \rho_{\downarrow\uparrow} \phi^*(t) & \rho_{\downarrow\downarrow} \end{bmatrix} \quad (2)$$

with the dephasing factor  $\phi(t) = \int p(\omega) \exp(-i\omega t) d\omega$  being the Fourier transform of  $p(\omega)$ .

Interestingly, the heuristic example shown in Eq. (2) provides further insights into the role played by HEs. On the one hand, the probability distribution  $p(\omega)$  completely determines the pure dephasing via the Fourier transform in Eq (2). Similar situations occur when one considers the case of multivariate probability distribution<sup>26,29</sup>. Therefore, the probability distribution  $p_\lambda$  encapsulated within a HE can be conceived as a characteristic representation of the incoherent dynamics, which is even faithful for the case of pure dephasing of any dimension<sup>26,27</sup>. This observation endows the probability distribution  $p_\lambda$  a new interpretation as a representation function of incoherent dynamics over the frequency domain, referred to as canonical Hamiltonian ensemble representation (CHER).

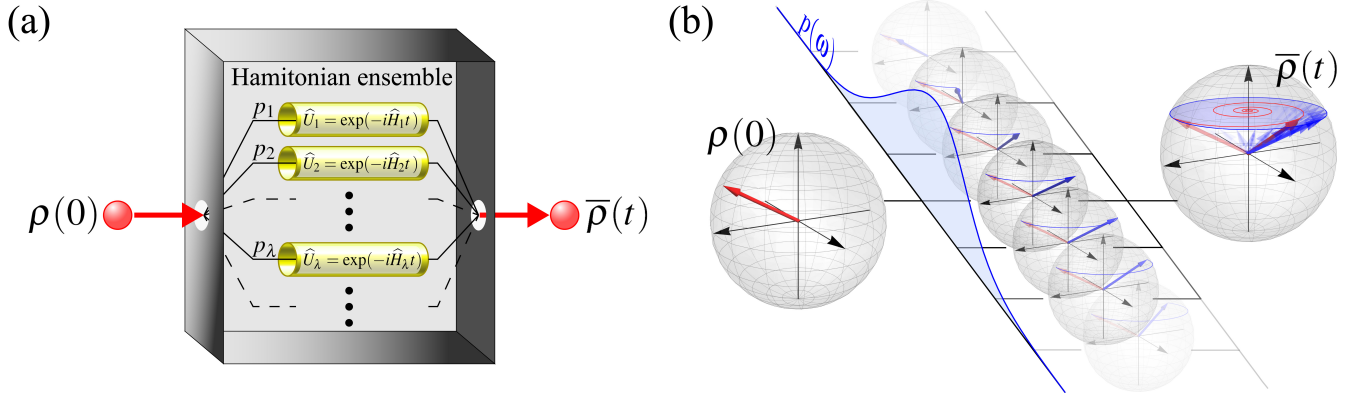


**Figure 1.** Schematic illustration of the ensemble-averaged dynamics under HEs. (a) A HE  $\{(p_\lambda, \hat{H}_\lambda)\}_\lambda$  consists of a collection of traceless Hermitian operators  $\hat{H}_\lambda \in \mathfrak{su}(n)$  associated with a probability  $p_\lambda$  of occurrence. An initial state  $\rho(0)$  will be randomly assigned to a certain unitary channel  $\hat{U}_\lambda(t) = \exp(-i\hat{H}_\lambda t)$  according to  $p_\lambda$ , giving rise to an ensemble-averaged dynamics  $\bar{\rho}(t)$  described by Eq. (1). (b) For the HE of spectral disorder  $\{(p(\omega), \omega\hat{\sigma}_z/2)\}_\omega$ , every unitary operator  $\exp(-i\omega\hat{\sigma}_z t/2)$  rotates the qubit state about the  $z$ -axis of the Bloch sphere at a fluctuating angular frequency  $\omega$ . Hence the qubit is subject to an uncertainty described by the probability distribution  $p(\omega)$ , and the ensemble-averaged dynamics  $\bar{\rho}(t)$  is a pure dephasing described by Eq. (2). The incoherent dynamical behavior is determined by  $p(\omega)$  via the Fourier transform  $\phi(t) = \int p(\omega) \exp(-i\omega t) d\omega$ .

On the other hand, since every unitary operator  $\exp(-i\omega\hat{\sigma}_z t/2)$  in Eq. (2) can be interpreted geometrically as a rotation about the  $z$ -axis of the Bloch sphere at angular frequency  $\omega$ , the pure dephasing is a result of the accumulation of a random phase, in line with the conventional interpretation of pure dephasing in the manner of the random phase model [figure 1(b)]. Consequently, the ensemble-averaged dynamics (1) under a HE can be considered as a statistical mixture of various unitary rotations weighted by  $p_\lambda$ . This underpins the classicality behind the HE.

## 2.2 Canonical Hamiltonian ensemble representation

Before further exploring the characterization of dynamical process nonclassicality with CHER, we elucidate how can a HE be recast into a Fourier transform using the formalism of group theory. This also strengthens the formal connection of the CHER to an incoherent dynamics beyond the above empirical observation.

As every member Hamiltonian operator  $\hat{H}_\lambda \in \mathfrak{su}(n)$  is Hermitian, it can be expressed as a linear combination

$$\hat{H}_\lambda = \sum_{m=1}^{n^2-1} \lambda_m \hat{L}_m = \vec{\lambda} \cdot \hat{L} \quad (3)$$

of  $n^2 - 1$  traceless Hermitian generators  $\hat{L}_m$  of  $\mathfrak{su}(n)$ . Therefore, the index  $\lambda$  parameterizing the HE is an  $(n^2 - 1)$ -dimensional real vector  $\vec{\lambda}$ . Here we restrict ourselves to traceless member Hamiltonian operators  $\hat{H}_\lambda$  without loss of generality, because the trace plays no role in the ensemble-averaged dynamics (1) due to the commutativity  $[\hat{I}, \hat{L}_m] = 0$  of the identity operator  $\hat{I}$  to all  $\hat{L}_m \in \mathfrak{su}(n)$ .

The commutator is critical for a Lie algebra as it determines many properties and the algebraic structure to a very large extent. For example, the generators of  $\mathfrak{su}(n)$  should satisfy  $[\hat{L}_k, \hat{L}_l] = i2c_{klm}\hat{L}_m$ , where the  $c_{klm}$ 's are called structure constants, satisfying the relation  $c_{klm} = -c_{lkm} = -c_{mlk}$ . Additionally, the

commutator can be used to induce the adjoint representation of  $\mathfrak{su}(n)$  of fundamental importance according to

$$ad : \widehat{L}_m \mapsto \widetilde{L}_m = [\widehat{L}_m, \quad ]. \quad (4)$$

Namely, the adjoint representation  $ad$  uniquely associates each generator  $\widehat{L}_m$  to an endomorphism  $\widetilde{L}_m : \mathfrak{u}(n) \rightarrow \mathfrak{u}(n)$  with its action defined by the commutator as  $\widetilde{L}_m\{\widetilde{L}_k\} := [\widehat{L}_m, \widetilde{L}_k]$ . Since each endomorphism  $\widetilde{L}_m$  itself is a linear map, it admits a matrix representation of  $n^2 \times n^2$  dimension with elements given by the structure constants and its action is described by the ordinary matrix multiplication. Furthermore, according to the linear combination (3) and the bilinearity of the commutator, each member Hamiltonian can be associated according to

$$ad : \widehat{H}_\lambda \mapsto \widetilde{H}_\lambda = [\widehat{H}_\lambda, \quad ] = \sum_{m=1}^{n^2-1} \lambda_m \widetilde{L}_m = \vec{\lambda} \cdot \widetilde{L}. \quad (5)$$

Along with the adjoint representation  $ad$ , one can show that the action of each single unitary channel in Eq. (1) can be recast into an exponential form with respect to the generators  $\widetilde{L}_m$  as

$$\exp(-i\widehat{H}_\lambda t)\rho \exp(i\widehat{H}_\lambda t) = \sum_{j=0}^{\infty} \frac{(-it)^j}{j!} [\widehat{H}_\lambda, \rho]_{(j)} = \exp(-i\vec{\lambda} \cdot \widetilde{L}t)\{\rho\}, \quad (6)$$

where the multiple-layer commutator is defined iteratively according to  $[\widehat{H}_\lambda, \rho]_{(j)} = [\widehat{H}_\lambda, [\widehat{H}_\lambda, \rho]_{(j-1)}]$  and  $[\widehat{H}_\lambda, \rho]_{(0)} = \rho$ .

From the above equations, for a given HE  $\{(p_\lambda, \widehat{H}_\lambda)\}_\lambda$ , we can recast<sup>26</sup> the right hand side of Eq. (1) into a Fourier transform expression from the probability distribution  $p_\lambda$ , on a locally compact group  $\mathcal{G}$  parameterized by  $\lambda = \vec{\lambda} \in \mathbb{R}^{n^2-1}$ , to the dynamical linear map  $\mathcal{E}_t^{(\widetilde{L})}$ :

$$\mathcal{E}_t^{(\widetilde{L})} = \int_{\mathcal{G}} p_\lambda \exp(-i\lambda \widetilde{L}t) d\lambda. \quad (7)$$

Meanwhile, the action of the incoherent dynamics  $\mathcal{E}_t$  on a density matrix  $\rho$  can be expressed in terms of ordinary matrix multiplication

$$\mathcal{E}_t\{\rho\} \Rightarrow \mathcal{E}_t^{(\widetilde{L})} \cdot \rho, \quad (8)$$

with  $\rho$  on the left hand side being an  $n \times n$  density matrix, while the one on the right hand side being an  $n^2$ -dimensional real vector  $\rho = \{n^{-1}, \vec{\rho}\}$  in the sense of the linear combination  $\rho = n^{-1}\widehat{I} + \vec{\rho} \cdot \widehat{L}$ .

In summary, Eq. (7) associates a probability distribution  $p_\lambda$  within a HE to the incoherent dynamics  $\mathcal{E}_t$  under HE, i.e.,

$$p_\lambda \mapsto \mathcal{E}_t^{(\widetilde{L})}, \quad (9)$$

via the Fourier transform using the formalism of group theory. This explicitly elucidates that the role of  $p_\lambda$  as a characteristic representation over the frequency domain for  $\mathcal{E}_t$ , referred to as CHER. Additionally, the particular versatility of CHER lies in characterizing and quantifying the dynamical process nonclassicality. To do this, we will replace the probability distribution  $p_\lambda$  with the quasi-distribution  $\wp_\lambda$ , to incorporate the possibility that  $\wp_\lambda$  may contain negative values, which serve as an indicator of the nonclassical nature in the dynamical process  $\mathcal{E}_t$ . The emergence of negative values will be clarified in the following discussion.

## 2.3 Dynamical process nonclassicality

Upon elucidating how a given HE induces an incoherent dynamics, we consider a reverse problem of simulating a given incoherent dynamics with HEs, which serves as the classical strategy in the characterization of dynamical process nonclassicality.

As discussed in the Introduction, the incoherent behavior of an open system dynamics is caused by the destruction of the correlations established during the system-environment interaction. However, these correlations are typically not fully accessible in an experiment; therefore, it is not feasible to precisely infer whether an incoherent behavior results from quantum or classical correlations. Whereas, the reduced system dynamics is, in principle, fully attainable with the technique of, e.g., quantum process tomography (QPT) experiments or theoretically solving a master equation<sup>60–62</sup>. Consequently, in our approach, we focus exclusively on the reduced system dynamics and ignore the obscure actual system-environment correlations; meanwhile we attempt to explain the dynamics classically with HE simulations.

The classicality behind the HE simulations can be understood by recalling that<sup>25</sup>, if the system and its environment can at most establish classical correlations, without quantum discord nor entanglement, during their interactions, then the reduced system dynamics corresponds to a HE. This means that, if a given incoherent dynamics admits a HE simulation, then one cannot tell it apart from a classical model reproducing exactly the same dynamics relying merely on classical correlations. In other words, the given incoherent behavior can be explained classically by a statistical mixture of a collection of unitary channels.

On the contrary, if one fails to construct the simulating HEs, then the incoherent dynamics should go beyond classical HEs, showcasing the nonclassicality of the dynamical process. The nonexistence of simulating HEs can be proven by the necessity to resort to a nonclassical HE accompanied by a negative quasi-distribution  $\wp_\lambda$ . This renders the CHER  $\wp_\lambda$  quite versatile, not only representing the incoherent dynamics but also characterizing the dynamical process nonclassicality.

The nonclassicality is defined from a quantum-information-theoretic perspective, i.e., the inference of nonclassical system-environment correlations. However, a quantum-dynamical viewpoint providing insights into the origin of nonclassicality is still obscure. In the following, we will discuss how to implement our approach with an authentic quantum system. This in turn reveals the mechanism of system-environment interactions giving rise to nonclassical dynamics and the classicality-nonclassicality transition caused by the environmental dynamics.

## 3 Dynamics of NV<sup>-</sup> centers

### 3.1 Theoretical model

A single negatively charged nitrogen-vacancy (NV<sup>-</sup>) center is a point defect in diamond consisting of a substitutional nitrogen (N) and a vacancy (V) in an adjacent lattice site [figure 2(a)]. The C<sub>3</sub> rotation axis defines an intrinsic z-axis for the electron spin. The NV<sup>-</sup> center has an electron spin  $S = 1$  triplet as its ground state with a zero-field splitting  $D/2\pi = 2.87$  GHz between sublevels  $m_S = 0$  and  $m_S = \pm 1$ . By applying an external magnetic field  $\vec{B}$ , the degeneracy between  $m_S = \pm 1$  can be lifted due to the Zeeman splitting [figure 2(b)]. Then the two different single spin transitions  $|0\rangle \leftrightarrow |\pm 1\rangle$  can be addressed by selective microwave (MW) excitations. The lattice sites are mostly occupied by the spinless <sup>12</sup>C nuclei [light gray spheres in figure 2(c)], while the electron spin decoherence is caused by the randomly distributed <sup>13</sup>C isotopes [dark gray spheres in figure 2(c)] with nuclear spin  $J = 1/2$ . The natural abundance of <sup>13</sup>C is about 1.1%, leading to a spin qubit relaxation time  $T_1$  in the order of milliseconds<sup>63,64</sup> and a dephasing time  $T_2^*$  of microseconds<sup>65–67</sup>. The <sup>13</sup>C concentration can even be depleted in isotopically purified samples to prolong the coherence time<sup>40–42</sup>.

In the presence of an external magnetic field  $\vec{B}$ , the total Hamiltonian  $\hat{H}_T = \hat{H}_{NV} + \hat{H}_C + \hat{H}_I$  consists

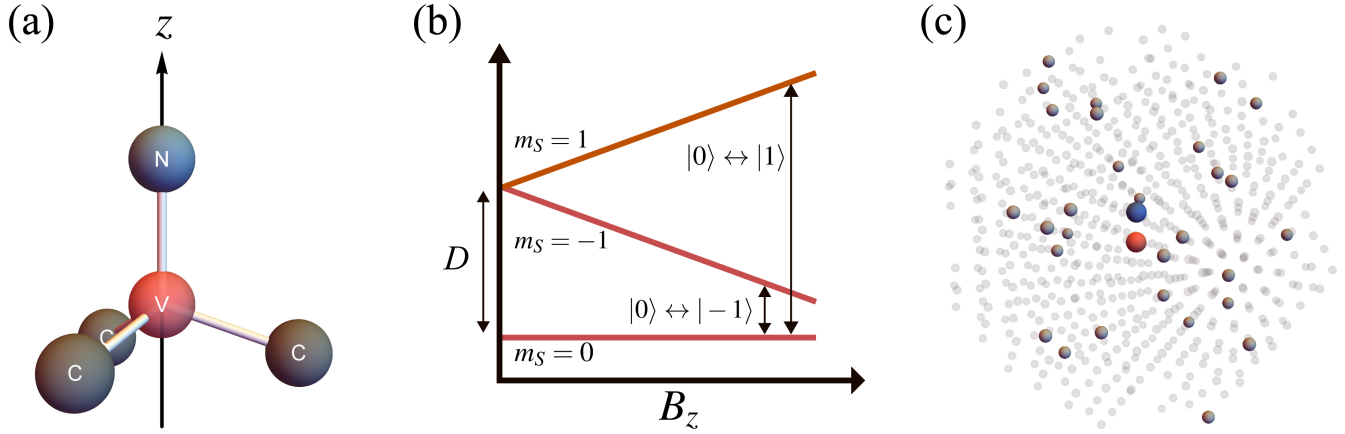


**Figure 2.** Atomic structure and ground state energy level of an  $\text{NV}^-$  center in a diamond lattice. (a) The atomic structure of an  $\text{NV}^-$  center in a diamond lattice, which consists of a substitutional nitrogen (N) and a vacancy (V) in an adjacent lattice site. The  $C_3$  rotation axis defines an intrinsic  $z$ -axis for the electron spin. (b) The ground state of the electron spin is a spin-1 triplet with a zero-field splitting  $D$  between sublevels  $m_S = 0$  and  $m_S = \pm 1$ . An external magnetic field will further lift the degeneracy between sublevels  $m_S = \pm 1$ . Then one can selectively address the two spin transitions  $|0\rangle \leftrightarrow |\pm 1\rangle$  with an appropriate MW pulse, forming a logical qubit. (c) The most abundant species in the diamond lattice is the spinless  $^{12}\text{C}$  nucleus (light gray sphere), which do not interact with the electron spin. The primary source of decoherence comes from the randomly distributed  $^{13}\text{C}$  isotopes (dark gray spheres) with nuclear spin  $J = 1/2$ . Due to the low concentration of  $^{13}\text{C}$  (1.1% natural abundance), the nuclear dipole-dipole interaction and the electron-nucleus Fermi contact are negligible.

of three terms. The first term describes the free Hamiltonian of the electron spin associated to the  $\text{NV}^-$  center,

$$\hat{H}_{\text{NV}} = D\hat{S}_z^2 + \gamma_e\vec{B} \cdot \hat{S}, \quad (10)$$

with  $D/2\pi = 2.87$  GHz being the zero-field splitting and  $\gamma_e/2\pi = 2.8025$  MHz/G the electron gyromagnetic ratio. The second term describes the nuclear spin bath consisting of  $^{13}\text{C}$  isotopes of  $J = 1/2$  indexed by  $k$ :

$$\hat{H}_{\text{C}} = \sum_k \gamma_{\text{C}}\vec{B} \cdot \hat{J}^{(k)}, \quad (11)$$

with  $\gamma_{\text{C}}/2\pi = 1.0704$  kHz/G being the gyromagnetic ratio of the  $^{13}\text{C}$  nuclei. Note that we have neglected the dipole-dipole interaction between  $^{13}\text{C}$  nuclei as its effect is much slower than the electron spin decoherence considered here. The last term  $\hat{H}_{\text{I}}$  takes into account the hyperfine coupling between electron spin and nuclear spin, which in general includes two contributions; namely, the Fermi contact and the dipole-dipole interaction. The former is proportional to the overlap of the electron wavefunction at the position of a nucleus. Since the electron wavefunction is highly localized at the defect, this effect is negligible for nuclei farther away than  $5 \text{ \AA}$  from the  $\text{NV}^-$  center. In our simulation, we have confirmed the relevance of the dipole-dipole hyperfine interaction as well as the negligibility of the Fermi contact by post-selecting a randomly generated configuration with all  $^{13}\text{C}$  nuclei lying outside this radius of  $5 \text{ \AA}$ . Therefore, we consider the dipole-dipole interaction to the  $k^{\text{th}}$  nucleus exclusively with

$$\hat{H}_{\text{I}} = \hat{S} \cdot \sum_k \vec{A}^{\leftrightarrow(k)} \cdot \hat{J}^{(k)}, \quad (12)$$

where the hyperfine coefficients are given by

$$A_{ij}^{(k)} = \alpha^{(k)} \left[ \vec{e}_i \cdot \vec{e}_j - 3(\vec{e}^{(k)} \cdot \vec{e}_i)(\vec{e}^{(k)} \cdot \vec{e}_j) \right] \quad (13)$$

with

$$\alpha^{(k)} = \frac{\mu_0 \gamma_e \gamma_C}{4\pi |\vec{r}^{(k)}|^3}, \quad (14)$$

$\mu_0$  the magnetic permeability of vacuum,  $\vec{r}^{(k)} = (r^{(k)} \sin \theta^{(k)} \cos \phi^{(k)}, r^{(k)} \sin \theta^{(k)} \sin \phi^{(k)}, r^{(k)} \cos \theta^{(k)})$  the displacement vector toward the  $k^{\text{th}}$  nucleus, and  $\vec{e}^{(k)}$  the unit vector of  $\vec{r}^{(k)}$ .

Additionally, since the  $\widehat{S}_z$  component is responsible for  $T_2^*$ , while the  $\widehat{S}_x$  and  $\widehat{S}_y$  components are for  $T_1$ , the experimentally measured three-order of magnitude difference between  $T_1$  and  $T_2^*$  guarantees a well-approximated pure dephasing of electron spin dynamics, on the time scale under study<sup>63–67</sup>. Therefore, it is relevant for us to neglect the terms proportional to  $\widehat{S}_x$  and  $\widehat{S}_y$  in Eq. (12) and consider only the  $\widehat{S}_z$  component phenomenologically. Meanwhile, assuming that an external magnetic field  $\vec{B} = B_z \vec{e}_z$  is aligned with the  $z$ -axis, then the total Hamiltonian can be expressed as

$$\widehat{H}_T = D \widehat{S}_z^2 + \gamma_e B_z \widehat{S}_z + \sum_k \gamma_C B_z \widehat{J}_z^{(k)} + \widehat{S}_z \sum_k \vec{A}_z^{(k)} \cdot \vec{J}^{(k)}. \quad (15)$$

And the three components of the hyperfine coefficients are explicitly written as

$$\begin{cases} A_{zx}^{(k)} = \alpha^{(k)} \left( -3 \cos \theta^{(k)} \sin \theta^{(k)} \cos \phi^{(k)} \right) \\ A_{zy}^{(k)} = \alpha^{(k)} \left( -3 \cos \theta^{(k)} \sin \theta^{(k)} \sin \phi^{(k)} \right) \\ A_{zz}^{(k)} = \alpha^{(k)} \left( 1 - 3 \cos^2 \theta^{(k)} \right) \end{cases} . \quad (16)$$

Due to the external magnetic field  $\vec{B} = B_z \vec{e}_z$  lifting the  $m_S = \pm 1$  degeneracy, now we selectively focus on the single-spin transition  $|0\rangle \leftrightarrow |1\rangle$ , forming a logical qubit. With this setup, the total Hamiltonian (15) is block diagonal in the electron spin basis in the form of

$$\widehat{H}_T = \sum_{m_S=0,1} |m_S\rangle \langle m_S| \otimes \widehat{H}_{m_S}, \quad (17)$$

with  $\widehat{H}_{m_S} = (m_S^2 D + m_S \gamma_e B_z) + \sum_k \vec{\Omega}_{m_S}^{(k)} \cdot \vec{J}^{(k)}$ ,  $\vec{\Omega}_0^{(k)} = \vec{\Omega}_0 = (0, 0, \gamma_C B_z)$ , and  $\vec{\Omega}_1^{(k)} = (A_{zx}^{(k)}, A_{zy}^{(k)}, A_{zz}^{(k)} + \gamma_C B_z)$ . Consequently, the corresponding total unitary time evolution operator

$$\widehat{U}_T(t) = \exp(-i\widehat{H}_T t) = \sum_{m_S=0,1} |m_S\rangle \langle m_S| \otimes \widehat{U}_{m_S}(t), \quad (18)$$

is also block diagonal in the electron spin basis with conditional evolution operators  $\widehat{U}_{m_S}(t) = \exp(-i\widehat{H}_{m_S} t)$ .

### 3.2 Pure dephasing dynamics of electron spin and nonclassicality

We now focus on the pure dephasing caused by the  $^{13}\text{C}$  nuclear spin bath during the free-induction-decay (FID) process. The initial state of total system is assumed to be a direct product of all subsystems

$$\rho_T(0) = \rho_{\text{NV}}(0) \otimes \prod_k \rho^{(k)}, \quad (19)$$



where  $\rho^{(k)} = [\widehat{I}^{(k)} + \vec{p}^{(k)} \cdot \widehat{\sigma}^{(k)}]/2$  is the initial state of the  $k^{\text{th}}$  nuclear spin with polarization  $\vec{p}^{(k)}$ , and  $\widehat{I}^{(k)}$  and  $\widehat{\sigma}^{(k)}$  are the identity and the Pauli operators, respectively, acting on the  $k^{\text{th}}$  nuclear spin Hilbert space. After being optically polarized to  $|0\rangle$ , the initial state of the electron spin is typically set to a balanced superposition  $(|0\rangle + |1\rangle)/\sqrt{2}$  by a  $\pi/2$  MW pulse in a conventional FID experiment. Then the electron-nucleus hyperfine interaction is turned on and the total system evolves unitarily according to  $\rho_{\text{T}}(t) = \widehat{U}_{\text{T}}(t)\rho_{\text{T}}(0)\widehat{U}_{\text{T}}^\dagger(t)$ , while the electron spin reduced density matrix  $\rho_{\text{NV}}(t) = \text{Tr}_{\text{C}}\rho_{\text{T}}(t)$  is obtained by tracing over the  $^{13}\text{C}$  nuclear spin bath.

The electron spin pure dephasing dynamics is characterized by the dephasing factor

$$\phi(t) = \langle 0|\rho_{\text{NV}}(t)|1\rangle = e^{i(D+\gamma_e B_z)t} \prod_k \text{Tr} \left[ \widehat{U}_1^{(k)\dagger}(t)\widehat{U}_0^{(k)}(t)\rho^{(k)} \right], \quad (20)$$

where  $\widehat{U}_0^{(k)}(t) = \exp[-i(\vec{\Omega}_0 \cdot \widehat{\sigma}^{(k)})t/2]$  and  $\widehat{U}_1^{(k)}(t) = \exp[-i(\vec{\Omega}_1^{(k)} \cdot \widehat{\sigma}^{(k)})t/2]$  gives rise to nuclear spin precession about the axis  $\vec{u}^{(k)} = \vec{\Omega}_1^{(k)}/|\vec{\Omega}_1^{(k)}|$  in the presence of the hyperfine field produced by the electron spin. Further details for the calculation of Eq. (20) are shown in [Appendix A](#).

In view of Eq. (2), to construct a simulating HE for the electron spin pure dephasing, each member Hamiltonian in the ensemble is of the form  $\omega\widehat{\sigma}_z/2$  and the CHER  $\wp(\omega)$  is determined by the inverse Fourier transform

$$\wp(\omega) = \frac{1}{2\pi} \int_{-\infty}^{\infty} \phi(t)e^{i\omega t} dt. \quad (21)$$

From Eq. (21), it is clear that the leading factor  $\exp[i(D + \gamma_e B_z)t]$  on the right hand side of Eq. (20) merely shifts  $\wp(\omega)$  by a displacement  $D + \gamma_e B_z$ , doing nothing to the profile of  $\wp(\omega)$  nor to the nonclassical signatures. Besides, we are interested in the effects caused by the nuclear spin bath while the leading factor is given by the energy space between the electron  $|0\rangle$  and  $|1\rangle$  states. Consequently, for our purpose, we can neglect the leading factor of Eq. (20) and explicitly write down the dephasing factor as

$$\begin{aligned} \phi(t) = \prod_k \left[ \left( \cos \frac{\Omega_0 t}{2} - ip_z^{(k)} \sin \frac{\Omega_0 t}{2} \right) \cos \frac{\Omega_1^{(k)} t}{2} + u_z^{(k)} \left( \sin \frac{\Omega_0 t}{2} + ip_z^{(k)} \cos \frac{\Omega_0 t}{2} \right) \sin \frac{\Omega_1^{(k)} t}{2} \right. \\ \left. + i \left( p_x^{(k)} u_x^{(k)} + p_y^{(k)} u_y^{(k)} \right) \cos \frac{\Omega_0 t}{2} \sin \frac{\Omega_1^{(k)} t}{2} + i \left( p_x^{(k)} u_y^{(k)} - p_y^{(k)} u_x^{(k)} \right) \sin \frac{\Omega_0 t}{2} \sin \frac{\Omega_1^{(k)} t}{2} \right]. \quad (22) \end{aligned}$$

Since the CHER  $\wp_\lambda$  is faithful for pure dephasing<sup>26,27</sup>, we can construct a quantitative measure of nonclassicality in accordance with the uniqueness of CHER for pure dephasing. Additionally, it is manifest that the classical CHERs form a convex set, i.e., the statistical mixture of classical CHERs is again a classical CHER, therefore an intuitive measure can be defined as the distance from a nonclassical  $\wp_\lambda$  to the classical set  $\mathcal{C}$  of the conventional probability distribution  $p_\lambda$ , which is given by<sup>26</sup>

$$\mathcal{N}\{\mathcal{E}_i\} = \inf_{p_\lambda \in \mathcal{C}} \int_{\mathcal{G}} \frac{1}{2} |\wp_\lambda - p_\lambda| d\lambda. \quad (23)$$

### 3.3 Nuclear spin polarization and precession

From Eq. (22), it is manifest that the polarization  $\vec{p}^{(k)}$  and the precession axis of the nuclear spin, described by  $\vec{u}^{(k)}$ , have significant influences on the electron spin dephasing dynamics. Therefore, it is possible to manipulate the dynamical behavior of the electron spin showing the transition between classicality and nonclassicality by engineering the nuclear spin bath.

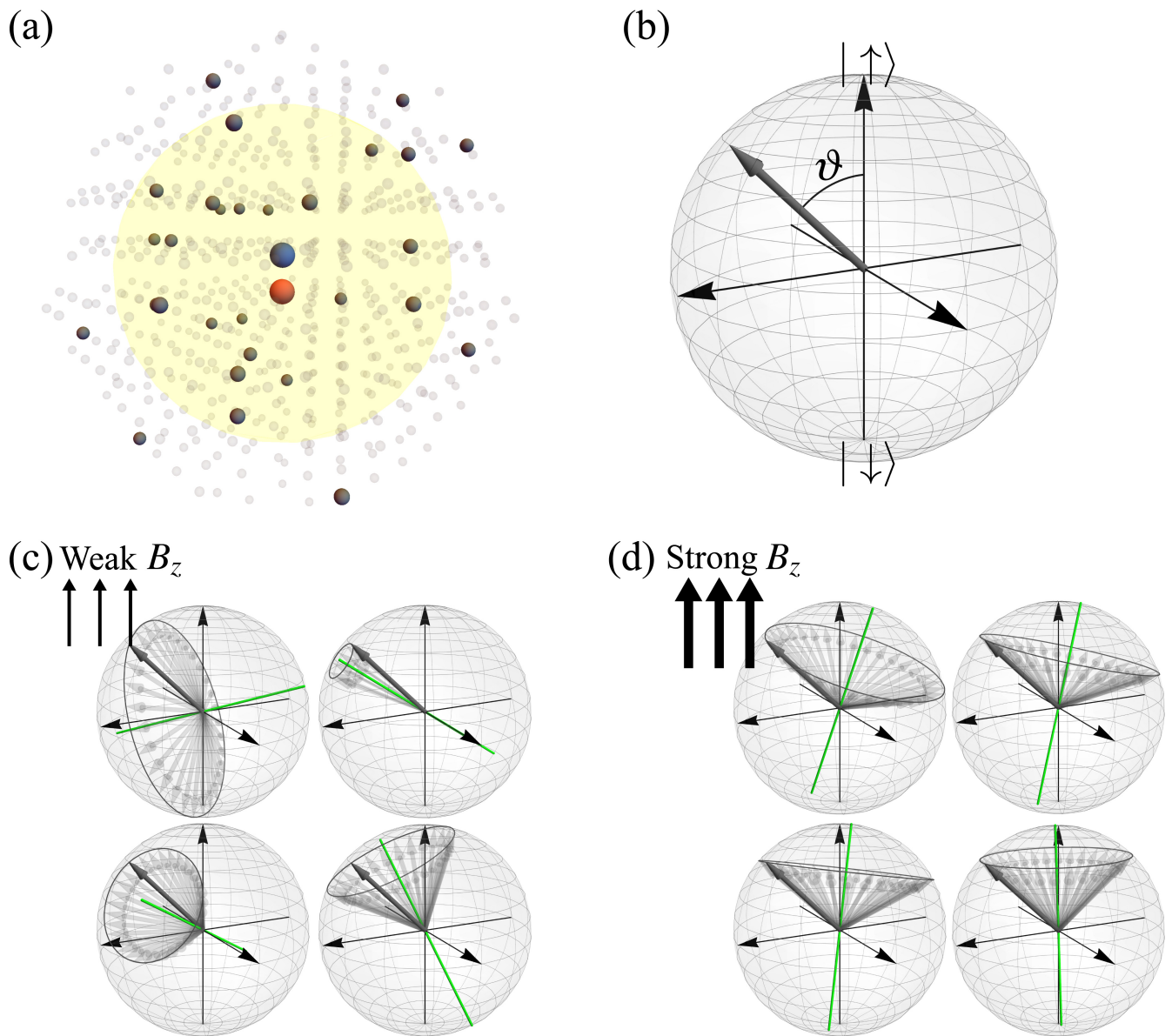


**Figure 3.** Polarization and precession of the nuclear spin bath. (a) DNP transfers electron spin polarization to the surrounding nuclear spins via the electron-nucleus hyperfine interaction. Only the nuclei within a polarization area (yellow spherical shadow) can be efficiently polarized via direct polarization transfer, achieving hyperpolarization. Therefore, we assume a polarization area of radius 1 nm and only the nuclei within this area can be identically polarized in a controllable manner. (b) We assume that the polarized nuclear spins within the polarization area are aligned in the  $x$ - $z$  plane with identical  $\vec{p}^{(k)} = (|\vec{p}| \sin \vartheta, 0, |\vec{p}| \cos \vartheta)$ . We will see that not only the magnitude  $|\vec{p}|$ , but also the orientation  $\vartheta$  have significant influence on the electron spin dynamics. (c) At weak fields, the axes of nuclear spin precessions (green axes) are randomly oriented due to the disordered  $^{13}\text{C}$  positions. (d) When the external field is increased, most of the axes are gradually tilted and finally aligned regularly, approaching the  $z$ -axis since  $\vec{\Omega}_1^{(k)}$ 's are dominated by the external field.

One of the mature approaches to engineer the bath is the dynamical nuclear polarization (DNP), which transfers the electron spin polarization to the surrounding nuclear spins via hyperfine interaction and

the resonance between them. Several approaches implementing DNP have been developed<sup>58,59,68–76</sup>. Among these DNP approaches, the polarization mechanisms, as well as the resulting performances, differ from each other. Generically, it is not feasible to polarize the whole nuclear spin bath; whereas, only a few number of nuclear spins within a polarization area, indicated by the yellow spherical shadow in figure 3(a), can be directly polarized and achieve hyperpolarization. The rest of the nuclear spins outside the polarization area have a vanishingly low magnitude of polarization. Therefore, we assume that only the nuclei within 1 nm from the electron spin possess identical and controllable polarization, i.e., finite  $\vec{p}^{(k)} = (|\vec{p}| \sin \vartheta, 0, |\vec{p}| \cos \vartheta)$  [figure 3(b)] for  $\vec{r}^{(k)} \leq 1$  nm; otherwise  $\vec{p} = 0$ . Moreover, not only the magnitude  $|\vec{p}|$ , but also the orientation  $\vartheta$ , are controllable.

The other one critical mechanism manipulating the FID classicality-nonclassicality transition is caused by the nuclear spin precession axes, which can be engineered by the external magnetic field  $B_z$ . This can be understood by observing that  $\vec{\Omega}_1^{(k)} = \vec{A}_z^{(k)} + \gamma_C B_z \vec{e}_z$ , and  $|\vec{A}_z^{(k)}| \propto |\vec{r}^{(k)}|^{-3}$ . At weak fields, most of the nuclear spin precession axes [green axes in figure 3(c)] are randomly oriented due to the randomly distributed  $^{13}\text{C}$  positions. Therefore, the electron spin will experience a highly disordered hyperfine field caused by the randomly oriented nuclear spin precessions and, consequently, the nonclassical trait is smeared.

On the other hand, when the external field is increasing, the Zeeman splitting  $\gamma_C B_z \vec{e}_z$  gradually dominates most of  $\vec{\Omega}_1^{(k)}$ . Consequently, most of the axes will tilt and finally align regularly, approaching the  $z$ -axis, i.e.,  $\vec{u}^{(k)} \approx \vec{e}_z$ , as shown in figure 3(d), resulting in a more coherence hyperfine field on the electron spin.

## 4 Numerical simulations

In our numerical simulations, we have generated a configuration of nuclear spins consisting of 520  $^{13}\text{C}$  nuclei randomly distributed over 47,231 lattice points, resulting in the natural abundance of 1.1%. Additionally, to confirm the relevance of the dipole-dipole hyperfine interaction in the interaction Hamiltonian (12), we have also verified that all  $^{13}\text{C}$  nuclei are farther away than 5 Å from the electron spin. After building an appropriately polarized nuclear spin bath, the magnetic field is set to be parallel to the  $z$ -axis at several different values.

We first show the numerical results of Eq. (22) in figure 4 for an unpolarized nuclear spin bath, i.e.,  $|\vec{p}| = 0$  for all nuclear spins, at various values of the magnetic field. The dynamical behavior of the dephasing factor is shown in figure 4(a). We can observe that, when the magnetic field is large enough, the sharp descent at the beginning becomes gentler, indicating an enhanced  $T_2^*$  time. This is in good agreement with an experimental report<sup>67</sup>, wherein a similar explanation in terms of a competition between  $\vec{A}_z^{(k)}$  and  $\gamma_C B_z \vec{e}_z$  was proposed for the enhanced  $T_2^*$ . It is also intriguing to note that there exists a crossover when  $B_z > 100$  G, which can be seen clearer from the profile of CHERs.

Figure 4(b) shows the corresponding CHERs  $\wp(\omega)$ , obtained from the inverse Fourier transform (21). For the case of an unpolarized nuclear spin bath, the profiles are symmetric and centered at  $\omega = 0$ . The symmetry of the profiles can be understood from the viewpoint that an unpolarized spin is a mixture of two opposite polarizations of the same magnitude, leading to two peaks at opposite positions as well as a symmetric CHER. In this case the CHERs are positive, indicating a classical-like dynamical behavior of electron spin.

Additionally, the aforementioned crossover is also clearer from the wavy profiles when  $B_z > 100$  G. The origin of this crossover can also be explained by the tilt of the precession axes illustrated in the previous section. At weak fields, the profile is relatively smooth with less peaks, resulting from the

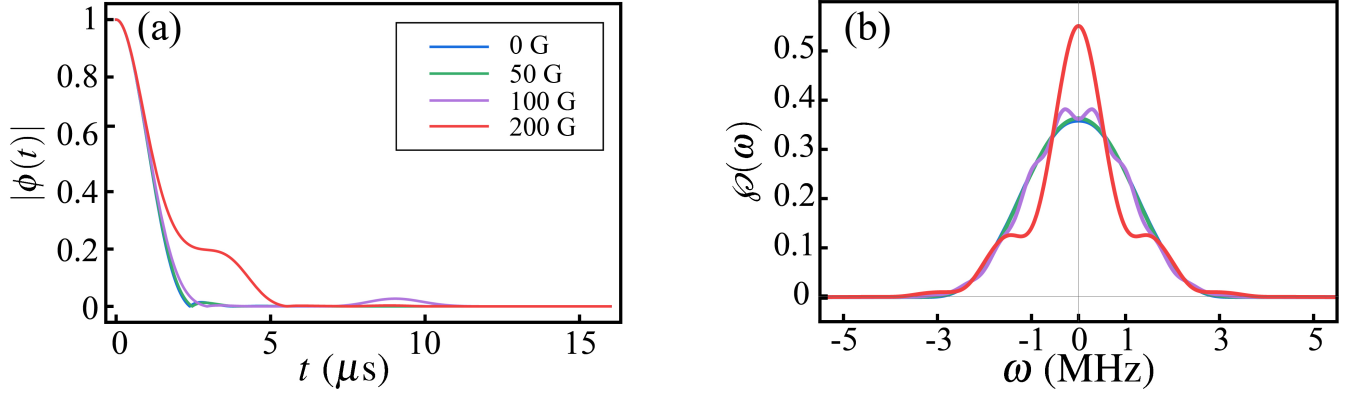


**Figure 4.** Dynamics and CHER of the electron spin for an unpolarized nuclear spin bath. (a) The dynamical behavior of dephasing factor for an unpolarized nuclear spin bath at various values of magnetic field. The sharp descent in the beginning becomes gentle at a large value of magnetic field, indicating an enhanced  $T_2^*$  time with increasing magnetic field. (b) The CHERs are symmetric since the nuclear spin bath is unpolarized. The positivity of the CHERs indicates that the electron spin behaves classically in an unpolarized spin bath. Additionally, the crossover, from a smooth curve to wavy profile, when  $B_z > 100$  G is easily observed. This is a result of the alignment of the tilted precession axes with increasing magnetic field.

randomly oriented precession axes. When the field is strong enough, the precession axes gradually tilt regularly toward the  $z$ -axis. Particularly, when  $B_z > 100$  G, even the nuclear spins within the polarization area, which have dominant impact on the electron spin, gradually tilt as well. Therefore, peaks emerge as the hyperfine fields caused by the tilted nuclear spins possess a consistent orientation, leading to wavy profiles.

We then proceed to investigate the impact of nuclear spin polarization on the electron spin dephasing dynamics. Figure 5 shows the results of polarization toward the  $z$ -axis, i.e.,  $\vartheta = 0$ , at magnitudes  $|\vec{p}| = 0.5$  (upper panels) and 1 (lower panels), respectively. From the dynamical behavior of the dephasing factor shown in figures 5(a) and (c), we can observe that the oscillating tail following the sharp descent at the beginning becomes stronger with increasing polarization magnitude  $|\vec{p}|$ , resulting in an enhanced  $T_2^*$  time as well. This is also in line with experimental reports<sup>58,59</sup> that the polarized nuclear spin toward the  $z$ -axis is capable of quenching the electron spin decoherence. Meanwhile, the oscillating amplitude is increasing at strong fields due to the alignment of the tilted nuclear spin precession axes, as schematically illustrated in figures 3(c) and (d).

The impact of nuclear spin polarization is even prominent on the profile of CHER shown in figures 5(b) and (d). In the presence of finite polarization, the mixture of two opposite polarizations is no longer balanced, giving rise to a bias in the profile of the CHER. Moreover, the almost regularly aligned precession axes at strong fields render specific peaks even sharper. On the other hand, it is worthwhile to note that, even if both the hyper- $z$ -polarization and the strong field manipulate the profile of CHER significantly, those shown in figures 5 are still positive without revealing a nonclassical trait.

We attribute this classicality to the extent of nuclear spin precession, which is a result of the alignment of the precession axes  $\vec{u}^{(k)}$  and the orientation of the polarization  $\vec{p}$ . It has been illustrated in the previous section that the precession axes gradually tilt regularly toward the  $z$ -axis, i.e.,  $\vec{u}^{(k)} \approx \vec{e}_z$ , with increasing magnetic field. Then, for the case of polarization toward the  $z$ -axis, the alignment of the precession axes renders most of the angles between  $\vec{u}^{(k)}$  and  $\vec{p}$  very small, and, consequently, most of the precession cones swept through by the nuclear spin are narrow [figure 6(a)]. Therefore, the electron spin will experience a

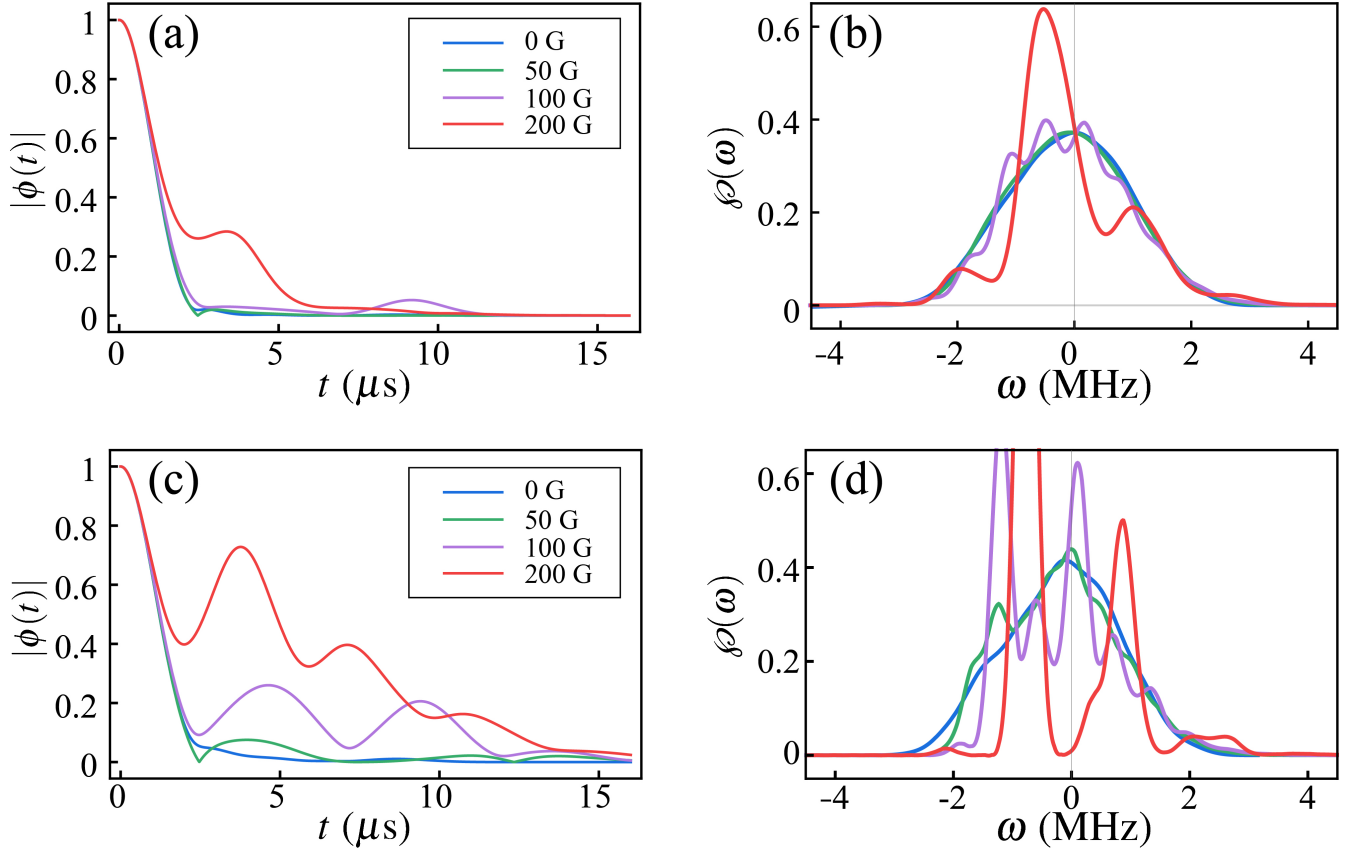


**Figure 5.** Dynamics and CHER of the electron spin for a  $z$ -polarized nuclear spin bath. The dynamical behavior (left panels) and the corresponding CHER (right panels) for the case of polarization toward the  $z$ -axis at magnitudes  $|\vec{p}| = 0.5$  [upper panels (a) and (b)] and 1 [lower panels (c) and (d)], respectively. From the dynamics shown in the left panels, we can observe that the sharp descent at the beginning is followed by a stronger oscillating tail with increasing polarization magnitude  $|\vec{p}|$ , resulting in an enhanced  $T_2^*$  time. This shows that the polarized nuclear spin toward the  $z$ -axis is capable of quenching the electron spin decoherence. Meanwhile, the oscillating amplitude is increasing at strong fields, reflecting the almost regular alignment of tilted nuclear spin precession axes. From the CHER shown in the right panels, the curves are pushed aside due to the polarized nuclear spin bath, leading to biased profiles. Notably, in the presence of both the hyper- $z$ -polarization and the strong field, the CHERs are positive without revealing a nonclassical trait.

relatively static hyperfine field caused by the precessionless nuclear spin bath and behave classical-like. On the other hand, if the polarization is set toward the  $x$ -axis, the nuclear spin precession dynamics will be significantly different. As shown in figure 6(b), the large angles between  $\vec{u}^{(k)}$  and  $\vec{p}$  will expand the precession cones, giving rise to a dynamic nuclear spin bath, as well as a dynamic hyperfine field experienced by the electron spin. Consequently, the electron spin will reveal a prominent nonclassical trait.

To investigate the nonclassicality induced by the aforementioned nuclear spin precession dynamics, we assume that the nuclear spins are polarized toward the  $x$ -axis, i.e.,  $\vartheta = \pi/2$ . The numerical results are shown in figure 7 with magnitudes  $|\vec{p}| = 0.5$  (upper panels) and 1 (lower panels), respectively. The dynamical behavior of the dephasing factor is shown in figures 7(a) and (c). In contrast to the case of  $z$ -polarization, the effect of prolonging the  $T_2^*$  time by increasing the magnitude of the  $x$ -polarization

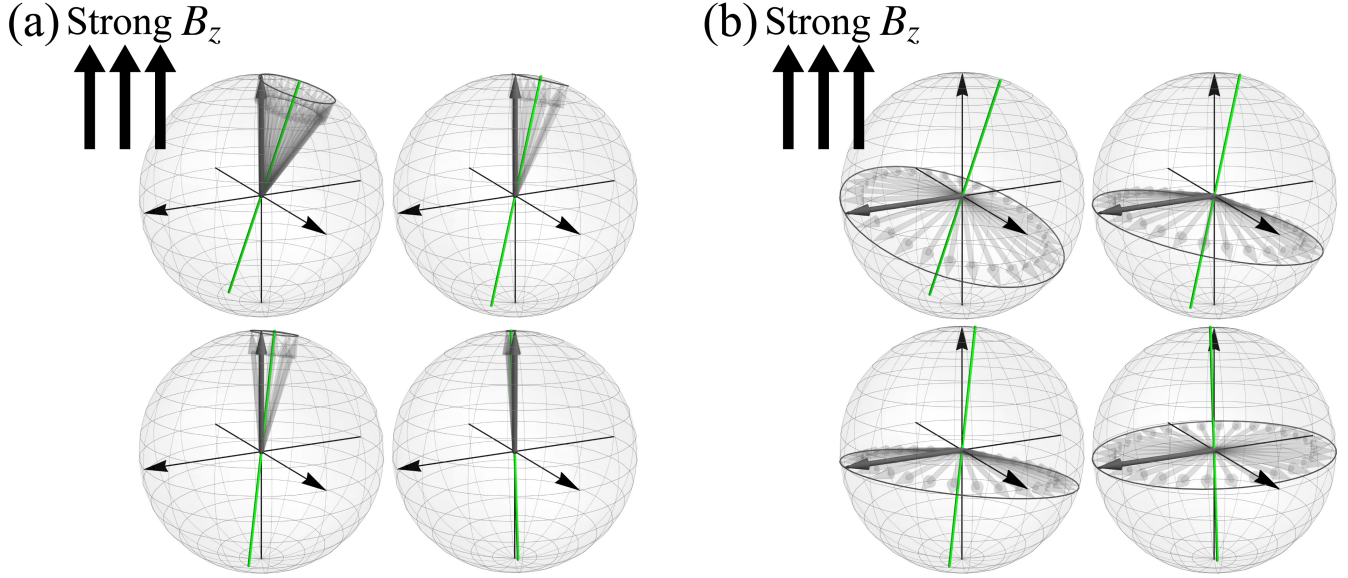


**Figure 6.** Nuclear spin precession dynamics. (a) For the case of polarization toward the  $z$ -axis, the almost regular alignment of the tilted nuclear spin precession axes at strong fields renders most of the angles between  $\vec{u}^{(k)}$  and  $\vec{p}$  very small. Therefore, most of the precession cones swept through by the nuclear spins are narrow, giving rise to a relatively static hyperfine field on the electron spin. (b) The polarization toward the  $x$ -axis expands the precession cones, giving rise to a dynamic nuclear spin bath. The electron spin will behave nonclassically under such dynamic hyperfine field.

is negligibly small. Additionally, the dependence of the oscillating amplitude on the external magnetic field is also seemingly nontrivial. On the other hand, it is heuristic to note that, even if the dynamical behavior is surely manipulated by the different types of polarization, generally speaking, the curves for different types of polarization share substantial similarities. In other words, the response of the curves to the different types of polarization is not qualitatively sensitive.

On the contrary, the situation is very different for CHERs. As shown in figures 7(b) and (d), rather than revealing a bias by pushing the curves aside caused by the  $z$ -polarization, the asymmetry raised by the  $x$ -polarization emerges in a manner of distortion. This means that the profile of CHER reflects the difference in the two types of nuclear spin precession dynamics illustrated in figure 6. Additionally, the most exotic property of the CHER raised by the  $x$ -polarization is the emergence of negative values, which is enhanced with both increasing  $B_z$  and  $|\vec{p}|$ . This, on the one hand, definitely certifies the nonclassicality of the electron spin pure dephasing dynamics in the presence of nuclear spin polarization toward the  $x$ -axis; on the other hand, we also showcase the versatility of the CHER as a probe of nuclear spin bath dynamics.

To quantitatively investigate the nonclassicality, we show the numerical results of nonclassicality  $\mathcal{N}$  quantified by Eq. (23) in figure 8. We first show the dependence on the magnitude  $|\vec{p}|$  in figure 8(a), where the polarization is set toward the  $x$ -axis and  $B_z = 200$  G. The nonclassicality is increasing with  $|\vec{p}|$ , consistent with what we have seen from the CHERs in the presence of  $x$ -polarized nuclear spins [figures 7(b) and (d)]. Figure 8(b) shows the dependence on the orientation  $\vartheta$  with  $|\vec{p}| = 1$  and  $B_z = 200$  G. When  $\vartheta = 0$ , the nuclear spins are  $z$ -polarized and the electron spin dynamics reveals a classical-like behavior. When the nuclear spins are gradually rotated toward the  $x$ -axis, the nonclassicality increases due to the mechanism of nuclear spin precession dynamics illustrated in figure 6(b). Finally, the overall response of the nonclassicality to the manipulation on the nuclear spin bath is shown in figure 8(c) with  $\vartheta = \pi/2$ . Both of the two experimentally controllable parameters  $B_z$  and  $|\vec{p}|$  manipulate the nuclear

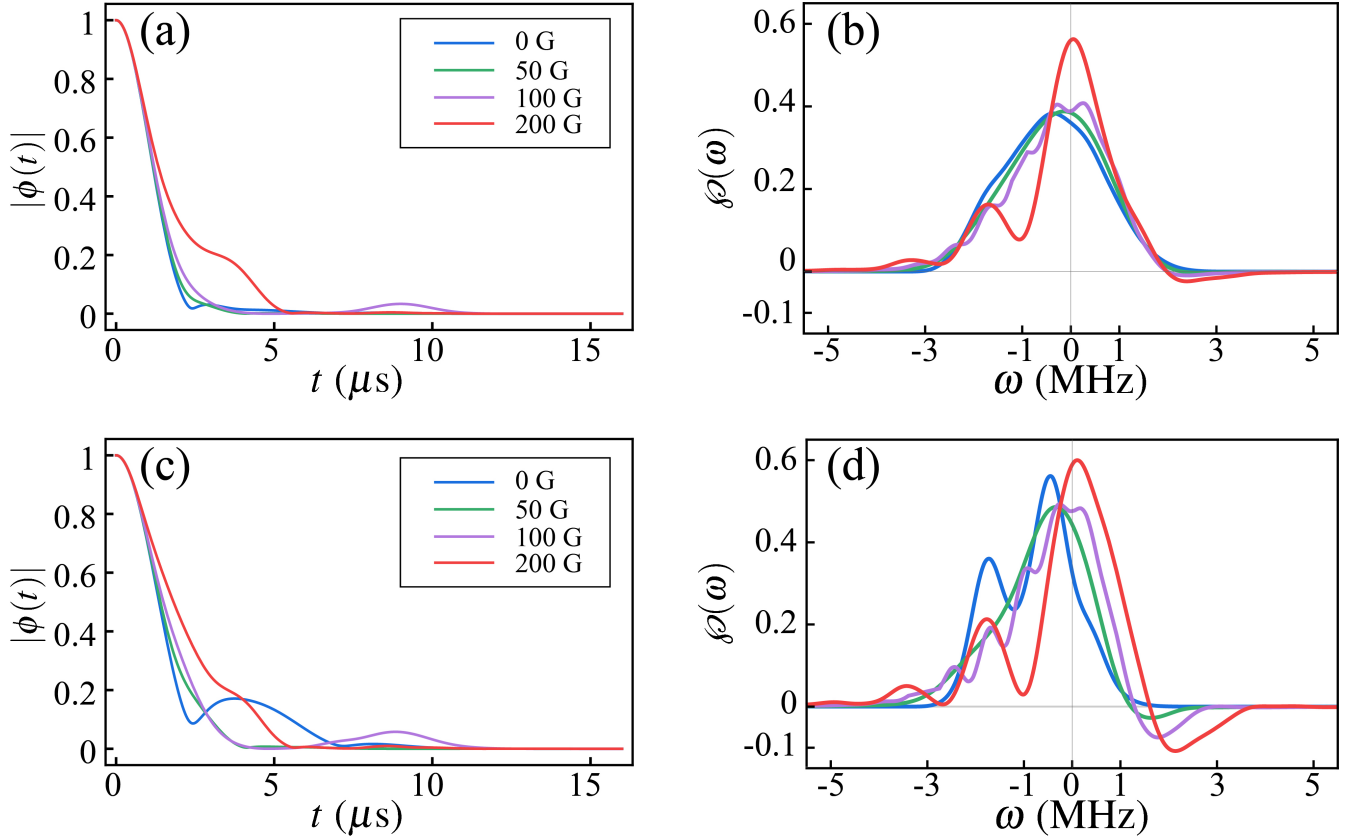


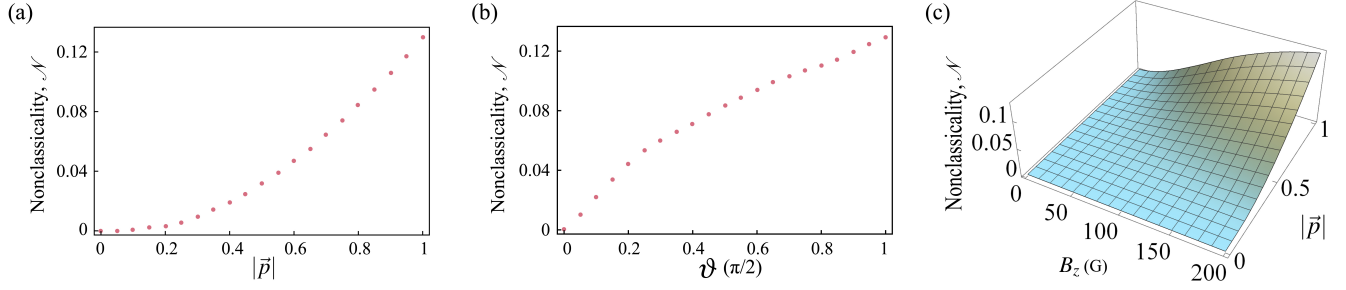
**Figure 7.** Dynamics and CHER of the electron spin for an  $x$ -polarized nuclear spin bath. The dynamical behavior (left panels) and the corresponding CHER (right panels) for the case of polarization toward the  $x$ -axis at magnitudes  $|\vec{p}| = 0.5$  [upper panels (a) and (b)] and 1 [lower panels (c) and (d)], respectively. The dynamical behavior shows a different response to the presence of  $x$ -polarization. It has negligibly small effects for prolonging the  $T_2^*$  time. Additionally, the dependence of the oscillating amplitude on the external magnetic field is nontrivial. On the contrary, the profiles of CHER show a qualitative difference from the case of  $z$ -polarization. The asymmetry of the profiles raised by the  $x$ -polarization emerges in a manner of distortion. Additionally, the most exotic property is the emergence of negative values, which is enhanced when increasing both  $B_z$  and  $|\vec{p}|$ . This is the crucial indicator of the nonclassical trait of the electron spin dynamics caused by the nuclear spin precession dynamics.

spin precession dynamics, which in turn induces nonclassicality in the electron spin dephasing dynamics. Consequently, the nonclassicality increases with  $B_z$  and  $|\vec{p}|$ .

## 5 Experimental proposal

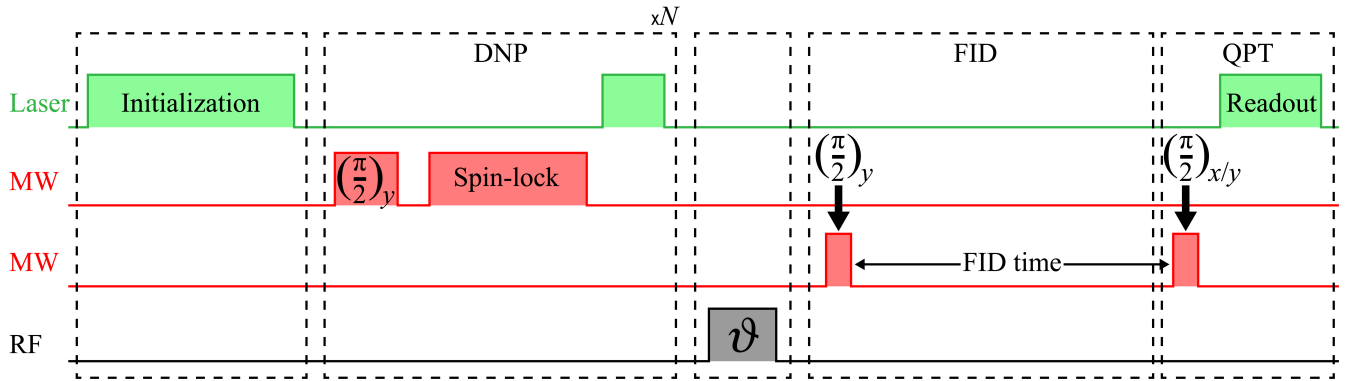
Finally, in order to underpin the experimental viability of our numerical simulation, we also propose an experimental pulse sequence for carrying out the model. We stress that all the necessary techniques included in this proposal are mature, up to an appropriate variation.

Figure 9 shows our proposal. The pulse sequence begins with an electron spin initialization to  $|0\rangle$  by a 532-nm green laser. Then the DNP is applied to transfer the electron spin polarization to the ambient nuclear spins. Several approaches implementing DNP have been developed<sup>58,59,68–76</sup>. A typical one, operating at a strong field with level anticrossing, begins with a  $(\pi/2)_y$  MW pulse rotating the electron



**Figure 8.** Variation of nonclassicality with different parameters. (a) The nonclassicality increases with magnitude  $|\vec{p}|$  of the polarization. In this plot we have set an  $x$ -polarized nuclear spin bath ( $\vartheta = \pi/2$ ) and  $B_z = 200$  G. (b) The nonclassicality increases with the orientation  $\vartheta$  of the polarization. Increasing  $\vartheta$  indicates that the nuclear spin bath is rotated from the  $z$ -axis toward the  $x$ -axis. In this plot we have assumed a hyperpolarization  $|\vec{p}| = 1$  and  $B_z = 200$  G. (c) This panel summarizes the overall response of the nonclassicality to the manipulation on the nuclear spin bath. The two experimentally controllable parameters,  $B_z$  and  $|\vec{p}|$ , denote two mechanisms of how we manipulate the nuclear spin precession dynamics, which in turn induces nonclassicality in the electron spin dephasing dynamics. Therefore, the nonclassicality increases with  $B_z$  and  $|\vec{p}|$ . In this plot we have set an  $x$ -polarized nuclear spin bath ( $\vartheta = \pi/2$ ).

spin about the  $y$ -axis to the  $x$  direction. A following pulse locks the spin along the  $x$  direction for a period, during which the electron spin polarization will transfer to the ambient nuclear spins. The last step of the DNP sequence is an additional green laser pulse polarizing the electron spin again. The DNP sequence will be repeated  $N$  times in order to build a hyperpolarized nuclear spin bath. After that, a radio-frequency (RF) pulse is applied to manipulate the orientation  $\vartheta$ . Finally, a Ramsey pulse sequence, operating at desired fields, is used to activate the FID process of the electron spin.



**Figure 9.** The proposed experimental pulse sequence for carrying out the model. After the electron spin initialization to  $|0\rangle$  by a 532-nm green laser, a repeated DNP sequence followed by a RF pulse is used to build a hyperpolarized nuclear spin bath toward the orientation  $\vartheta$ . Finally, a variant Ramsey sequence with two alternative final  $(\pi/2)_{x/y}$  MW pulses can gather the signals of the imaginary and real parts of the dephasing factor  $\phi(t)$ , respectively, fulfilling the requirement of QPT.

Crucially, to implement the CHER theory, one should experimentally reconstruct the dynamical linear map  $\mathcal{E}_t^{(L)}$  in Eq. (7), which requires a full QPT experiment to gather necessary information on the qubit dynamics. However, the conventional Ramsey sequence is clearly insufficient for QPT. Due to the pure



dephasing dynamical behavior of the electron spin, we propose a variant Ramsey sequence with two alternative final  $(\pi/2)_{x/y}$  MW pulses before the optical readout. These two readout signals correspond to the imaginary and real parts of the dephasing factor  $\phi(t)$ , respectively, fulfilling the requirement of QPT.

## 6 Conclusions

In conclusion, we have analyzed the pure dephasing dynamics and the corresponding CHER with an authentic quantum system of an  $NV^-$  center. By engineering the nuclear spin precession dynamics, on the one hand, we can manipulate the dynamical behavior of the electron spin showing the transition between classicality and nonclassicality during the FID process; on the other hand, we have also investigated the process nonclassicality from a new viewpoint of quantum-dynamical mechanism, rather than the original quantum-information-theoretic perspective. This reveals not only how the nuclear spin precession dynamics gives rise to the nonclassical trait in the electron spin FID process, but also the role played by the environmental dynamics in the origin of dynamical process nonclassicality.

Following the logic of the violation of Bell's inequality or the negativity in the phase space representation of a bosonic field, the nonclassicality characterized by the CHER is based on the failure of a classical strategy formulated in terms of HEs, which is shown to be closely related to the nonclassical correlations between the system and its environment. By further recasting the ensemble-averaged dynamics under a HE into a Fourier transform using the formalism of group theory, the role played by the CHER as a characteristic representation of a dynamical process over the frequency domain becomes manifest. Then we can quantitatively define the dynamical process nonclassicality in view of the negativity in the CHER.

We have applied the CHER theory to the FID process of the electron spin associated to an  $NV^-$  center in the diamond lattice and discovered how the nonclassicality is induced by the nuclear spin precession dynamics. There are two experimentally mature approaches engineering the nuclear spin precession dynamics, i.e., the external magnetic field and the DNP. The former tends to rotate the precession axes via a competition with the randomly oriented hyperfine interaction. At strong fields, most of the precession axes are regularly aligned along the  $z$ -axis, resulting in a more coherent hyperfine field experienced by the electron spin. While the latter transfers electron spin polarization to the surrounding nuclear spins within a polarization area and establishes hyperpolarization.

Here we have assumed a polarization area of radius 1 nm. For the case of polarization toward the  $z$ -axis at strong fields, most of the precession cones swept through by the nuclear spins are narrow, giving rise to a relatively static hyperfine field on the electron spin. If the nuclear spin polarizations are rotated toward the  $x$ -axis, the precession cones are expanded, giving rise to a dynamic nuclear spin bath. We found that the electron spin will behave nonclassically under a dynamic hyperfine field caused by the expanded precession cones.

This can be seen from the numerical simulations. The increasing magnetic field and  $z$ -polarization both can be used to enhance the  $T_2^*$  time, in good agreement with experimental reports. While the CHER will show a crossover from a smooth curve to wavy profile with increasing field and an asymmetry with larger polarization magnitude. Additionally, even in the presence of both the hyper- $z$ -polarization and the strong fields the CHER is positive, indicating a classical-like electron spin FID process. On the other hand, in the case of  $x$ -polarized nuclear spin bath, the dynamic hyperfine field caused by the nuclear spin precession gives rise to prominent negativity in the corresponding CHER. However, the  $x$ -polarization is not capable of enhancing the  $T_2^*$  time significantly. Consequently, we conclude that the nonclassicality will be stronger with increasing magnetic field and  $x$ -polarization. Finally, we also present an experimental pulse sequence for carrying out the model. Our proposal combines several mature techniques, including optical initialization and readout of electron spin, DNP, FID, and QPT.

## Data availability statement

The data that support the findings of this study are available upon reasonable request from the corresponding authors.

## Acknowledgments

This work is supported by the Ministry of Science and Technology, Taiwan, Grants No. MOST 108-2112-M-006-020-MY2, MOST 109-2112-M-006-012, MOST 110-2112-M-006-012, and MOST 111-2112-M-006-015-MY3, and partially by Higher Education Sprout Project, Ministry of Education to the Headquarters of University Advancement at NCKU. F.N. is supported in part by Nippon Telegraph and Telephone Corporation (NTT) Research, the Japan Science and Technology Agency (JST) [via the Quantum Leap Flagship Program (Q-LEAP), and the Moonshot R&D Grant Number JPMJMS2061], the Japan Society for the Promotion of Science (JSPS) [via the Grants-in-Aid for Scientific Research (KAKENHI) Grant No. JP20H00134], the Army Research Office (ARO) (Grant No. W911NF-18-1-0358), the Asian Office of Aerospace Research and Development (AOARD) (via Grant No. FA2386-20-1-4069), and the Foundational Questions Institute Fund (FQXi) via Grant No. FQXi-IAF19-06.

## Appendix A Derivation of the electron spin dephasing factor

Here we show how to obtain the expression for the dephasing factor (22) from Eq. (20). We consider the qubit manifold defined by the  $|0\rangle \leftrightarrow |1\rangle$  transition. Then the block diagonal total Hamiltonian (17) leads to a block diagonal unitary time evolution operator  $\hat{U}_T(t) = \exp(-i\hat{H}_T t) = |0\rangle\langle 0| \otimes \hat{U}_0 + |1\rangle\langle 1| \otimes \hat{U}_1$ , where

$$\begin{cases} \hat{U}_1 = \exp[-i(D + \gamma_e B_z)t] \prod_k \exp[-i(\vec{\Omega}_1^{(k)} \cdot \hat{\sigma}^{(k)})t/2] \\ \hat{U}_0 = \prod_k \exp[-i(\vec{\Omega}_0 \cdot \hat{\sigma}^{(k)})t/2] \end{cases}, \quad (24)$$

where  $\vec{\Omega}_1^{(k)} = (A_{zx}^{(k)}, A_{zy}^{(k)}, A_{zz}^{(k)} + \gamma_C B_z)$ , and  $\vec{\Omega}_0 = (0, 0, \gamma_C B_z)$ . Then the electron spin reduced density matrix

$$\rho_{NV}(t) = \text{Tr}_C[\hat{U}_T(t)\rho_T(0)\hat{U}_T^\dagger(t)] \quad (25)$$

is obtained by tracing over the  $^{13}\text{C}$  nuclear spin bath from the total density matrix.

Neglecting the internuclear initial correlations by considering the initial state  $\rho_T(0) = \rho_{NV}(0) \otimes \prod_k \rho^{(k)}$  with the nuclear spin initial state  $\rho^{(k)} = [\hat{I}^{(k)} + \vec{p}^{(k)} \cdot \hat{\sigma}^{(k)}]/2$ , then the dephasing factor

$$\phi(t) = \langle 0|\rho_{NV}(t)|1\rangle = \exp[i(D + \gamma_e B_z)t] \prod_k \text{Tr} \left[ \hat{U}_1^{(k)\dagger}(t) \hat{U}_0^{(k)}(t) \rho^{(k)} \right] \quad (26)$$

is given by a product of the effect of each single nuclear spin. To calculate  $\phi(t)$ , recall that

$$\begin{cases} \hat{U}_1^{(k)}(t) = \exp[-i(\vec{\Omega}_1^{(k)} \cdot \hat{\sigma}^{(k)})t/2] = \cos(\Omega_1^{(k)} t/2) \hat{I}^{(k)} - i \sin(\Omega_1^{(k)} t/2) (\vec{u}^{(k)} \cdot \hat{\sigma}^{(k)}) \\ \hat{U}_0^{(k)}(t) = \exp[-i(\vec{\Omega}_0 \cdot \hat{\sigma}^{(k)})t/2] = \cos(\Omega_0 t/2) \hat{I}^{(k)} - i \sin(\Omega_0 t/2) (\vec{e}_z \cdot \hat{\sigma}^{(k)}) \end{cases}. \quad (27)$$

Additionally, with the help of the prescription  $(\vec{u} \cdot \hat{\sigma})(\vec{v} \cdot \hat{\sigma}) = (\vec{u} \cdot \vec{v}) \hat{I} + i(\vec{u} \times \vec{v}) \cdot \hat{\sigma}$ , we have

$$\begin{aligned} \hat{U}_1^{(k)\dagger}(t) \hat{U}_0^{(k)}(t) &= \left( \cos \frac{\Omega_0 t}{2} \cos \frac{\Omega_1^{(k)} t}{2} + \sin \frac{\Omega_0 t}{2} \sin \frac{\Omega_1^{(k)} t}{2} \vec{u}^{(k)} \cdot \vec{e}_z \right) \hat{I}^{(k)} + i \sin \frac{\Omega_0 t}{2} \sin \frac{\Omega_1^{(k)} t}{2} (\vec{u}^{(k)} \times \vec{e}_z) \cdot \hat{\sigma}^{(k)} \\ &\quad + i \cos \frac{\Omega_0 t}{2} \sin \frac{\Omega_1^{(k)} t}{2} (\vec{u}^{(k)} \cdot \hat{\sigma}^{(k)}) - i \sin \frac{\Omega_0 t}{2} \cos \frac{\Omega_1^{(k)} t}{2} (\vec{e}_z \cdot \hat{\sigma}^{(k)}). \end{aligned} \quad (28)$$

Due to the orthogonality of the identity and the Pauli operators  $\text{Tr} \hat{\sigma}_j \hat{\sigma}_k = 2\delta_{jk}$ , the trace taken over the Hilbert space of the  $k^{\text{th}}$  nuclear spin is easy to perform. Then we obtain the desired result:

$$\phi(t) = e^{i(D+\gamma_e B_z)t} \prod_k \left[ \left( \cos \frac{\Omega_0 t}{2} - i p_z^{(k)} \sin \frac{\Omega_0 t}{2} \right) \cos \frac{\Omega_1^{(k)} t}{2} + u_z^{(k)} \left( \sin \frac{\Omega_0 t}{2} + i p_z^{(k)} \cos \frac{\Omega_0 t}{2} \right) \sin \frac{\Omega_1^{(k)} t}{2} \right. \\ \left. + i \left( p_x^{(k)} u_x^{(k)} + p_y^{(k)} u_y^{(k)} \right) \cos \frac{\Omega_0 t}{2} \sin \frac{\Omega_1^{(k)} t}{2} + i \left( p_x^{(k)} u_y^{(k)} - p_y^{(k)} u_x^{(k)} \right) \sin \frac{\Omega_0 t}{2} \sin \frac{\Omega_1^{(k)} t}{2} \right]. \quad (29)$$

Finally, neglecting the leading factor leads to Eq. (22).

## References

1. Ballentine, L. E. The statistical interpretation of quantum mechanics. Rev. Mod. Phys. **42**, 358–381, DOI: [10.1103/RevModPhys.42.358](https://doi.org/10.1103/RevModPhys.42.358) (1970).
2. Zurek, W. H. Decoherence, einselection, and the quantum origins of the classical. Rev. Mod. Phys. **75**, 715–775, DOI: [10.1103/RevModPhys.75.715](https://doi.org/10.1103/RevModPhys.75.715) (2003).
3. Schlosshauer, M. Decoherence, the measurement problem, and interpretations of quantum mechanics. Rev. Mod. Phys. **76**, 1267–1305, DOI: [10.1103/RevModPhys.76.1267](https://doi.org/10.1103/RevModPhys.76.1267) (2005).
4. Modi, K., Brodutch, A., Cable, H., Paterek, T. & Vedral, V. The classical-quantum boundary for correlations: Discord and related measures. Rev. Mod. Phys. **84**, 1655–1707, DOI: [10.1103/RevModPhys.84.1655](https://doi.org/10.1103/RevModPhys.84.1655) (2012).
5. Aspect, A., Grangier, P. & Roger, G. Experimental tests of realistic local theories via Bell’s theorem. Phys. Rev. Lett. **47**, 460–463, DOI: [10.1103/PhysRevLett.47.460](https://doi.org/10.1103/PhysRevLett.47.460) (1981).
6. Hensen, B. et al. Loophole-free Bell inequality violation using electron spins separated by 1.3 kilometres. Nature **526**, 682, DOI: [10.1038/nature15759](https://doi.org/10.1038/nature15759) (2015).
7. Giustina, M. et al. Significant-loophole-free test of Bell’s theorem with entangled photons. Phys. Rev. Lett. **115**, 250401, DOI: [10.1103/PhysRevLett.115.250401](https://doi.org/10.1103/PhysRevLett.115.250401) (2015).
8. Shalm, L. K. et al. Strong loophole-free test of local realism. Phys. Rev. Lett. **115**, 250402, DOI: [10.1103/PhysRevLett.115.250402](https://doi.org/10.1103/PhysRevLett.115.250402) (2015).
9. Bell, J. S. On the Einstein Podolsky Rosen paradox. Physics **1**, 195–200, DOI: [10.1103/PhysicsPhysiqueFizika.1.195](https://doi.org/10.1103/PhysicsPhysiqueFizika.1.195) (1964).
10. Brunner, N., Cavalcanti, D., Pironio, S., Scarani, V. & Wehner, S. Bell nonlocality. Rev. Mod. Phys. **86**, 419–478, DOI: [10.1103/RevModPhys.86.419](https://doi.org/10.1103/RevModPhys.86.419) (2014).
11. Wigner, E. P. On the quantum correction for thermodynamic equilibrium. Phys. Rev. **40**, 749–759, DOI: [10.1103/PhysRev.40.749](https://doi.org/10.1103/PhysRev.40.749) (1932).
12. Glauber, R. J. Coherent and incoherent states of the radiation field. Phys. Rev. **131**, 2766–2788, DOI: [10.1103/PhysRev.131.2766](https://doi.org/10.1103/PhysRev.131.2766) (1963).
13. Sudarshan, E. C. G. Equivalence of semiclassical and quantum mechanical descriptions of statistical light beams. Phys. Rev. Lett. **10**, 277–279, DOI: [10.1103/PhysRevLett.10.277](https://doi.org/10.1103/PhysRevLett.10.277) (1963).
14. Miranowicz, A., Bartkowiak, M., Wang, X., Liu, Y.-X. & Nori, F. Testing nonclassicality in multimode fields: A unified derivation of classical inequalities. Phys. Rev. A **82**, 013824, DOI: [10.1103/PhysRevA.82.013824](https://doi.org/10.1103/PhysRevA.82.013824) (2010).

15. Bartkowiak, M. et al. Sudden vanishing and reappearance of nonclassical effects: General occurrence of finite-time decays and periodic vanishings of nonclassicality and entanglement witnesses. Phys. Rev. A **83**, 053814, DOI: [10.1103/PhysRevA.83.053814](https://doi.org/10.1103/PhysRevA.83.053814) (2011).
16. Miranowicz, A. et al. Statistical mixtures of states can be more quantum than their superpositions: Comparison of nonclassicality measures for single-qubit states. Phys. Rev. A **91**, 042309, DOI: [10.1103/PhysRevA.91.042309](https://doi.org/10.1103/PhysRevA.91.042309) (2015).
17. Miranowicz, A., Bartkiewicz, K., Lambert, N., Chen, Y.-N. & Nori, F. Increasing relative nonclassicality quantified by standard entanglement potentials by dissipation and unbalanced beam splitting. Phys. Rev. A **92**, 062314, DOI: [10.1103/PhysRevA.92.062314](https://doi.org/10.1103/PhysRevA.92.062314) (2015).
18. Lambert, N., Emary, C., Chen, Y.-N. & Nori, F. Distinguishing quantum and classical transport through nanostructures. Phys. Rev. Lett. **105**, 176801, DOI: [10.1103/PhysRevLett.105.176801](https://doi.org/10.1103/PhysRevLett.105.176801) (2010).
19. Rahimi-Keshari, S. et al. Quantum process nonclassicality. Phys. Rev. Lett. **110**, 160401, DOI: [10.1103/PhysRevLett.110.160401](https://doi.org/10.1103/PhysRevLett.110.160401) (2013).
20. Sabapathy, K. K. Process output nonclassicality and nonclassicality depth of quantum-optical channels. Phys. Rev. A **93**, 042103, DOI: [10.1103/PhysRevA.93.042103](https://doi.org/10.1103/PhysRevA.93.042103) (2016).
21. Hsieh, J.-H., Chen, S.-H. & Li, C.-M. Quantifying quantum-mechanical processes. Sci. Rep. **7**, 13588, DOI: [10.1038/s41598-017-13604-9](https://doi.org/10.1038/s41598-017-13604-9) (2017).
22. Knee, G. C., Marcus, M., Smith, L. D. & Datta, A. Subtleties of witnessing quantum coherence in nonisolated systems. Phys. Rev. A **98**, 052328, DOI: [10.1103/PhysRevA.98.052328](https://doi.org/10.1103/PhysRevA.98.052328) (2018).
23. Smirne, A., Egloff, D., Díaz, M. G., Plenio, M. B. & Huelga, S. F. Coherence and non-classicality of quantum Markov processes. Quantum Sci. Technol. **4**, 01LT01, DOI: [10.1088/2058-9565/aeabd5](https://doi.org/10.1088/2058-9565/aeabd5) (2019).
24. Seif, A., Wang, Y.-X. & Clerk, A. A. Distinguishing between quantum and classical Markovian dephasing dissipation. Phys. Rev. Lett. **128**, 070402, DOI: [10.1103/PhysRevLett.128.070402](https://doi.org/10.1103/PhysRevLett.128.070402) (2022).
25. Chen, H.-B., Gneiting, C., Lo, P.-Y., Chen, Y.-N. & Nori, F. Simulating open quantum systems with Hamiltonian ensembles and the nonclassicality of the dynamics. Phys. Rev. Lett. **120**, 030403, DOI: [10.1103/PhysRevLett.120.030403](https://doi.org/10.1103/PhysRevLett.120.030403) (2018).
26. Chen, H.-B. et al. Quantifying the nonclassicality of pure dephasing. Nat. Commun. **10**, 3794, DOI: [10.1038/s41467-019-11502-4](https://doi.org/10.1038/s41467-019-11502-4) (2019).
27. Chen, H.-B. & Chen, Y.-N. Canonical Hamiltonian ensemble representation of dephasing dynamics and the impact of thermal fluctuations on quantum-to-classical transition. Sci. Rep. **11**, 10046, DOI: [10.1038/s41598-021-89400-3](https://doi.org/10.1038/s41598-021-89400-3) (2021).
28. Kropf, C. M., Gneiting, C. & Buchleitner, A. Effective dynamics of disordered quantum systems. Phys. Rev. X **6**, 031023, DOI: [10.1103/PhysRevX.6.031023](https://doi.org/10.1103/PhysRevX.6.031023) (2016).
29. Chen, H.-B. Effects of symmetry breaking of the structurally-disordered Hamiltonian ensembles on the anisotropic decoherence of qubits. Sci. Rep. **12**, 2869, DOI: [10.1038/s41598-022-06891-4](https://doi.org/10.1038/s41598-022-06891-4) (2022).
30. Gneiting, C., Anger, F. R. & Buchleitner, A. Incoherent ensemble dynamics in disordered systems. Phys. Rev. A **93**, 032139, DOI: [10.1103/PhysRevA.93.032139](https://doi.org/10.1103/PhysRevA.93.032139) (2016).

31. Kropf, C. M., Shatokhin, V. N. & Buchleitner, A. Open system model for quantum dynamical maps with classical noise and corresponding master equations. *Open Syst. Inf. Dyn.* **24**, 1740012, DOI: [10.1142/S1230161217400121](https://doi.org/10.1142/S1230161217400121) (2017).
32. Gneiting, C. & Nori, F. Disorder-induced dephasing in backscattering-free quantum transport. *Phys. Rev. Lett.* **119**, 176802, DOI: [10.1103/PhysRevLett.119.176802](https://doi.org/10.1103/PhysRevLett.119.176802) (2017).
33. Kropf, C. M. Protecting quantum coherences from static noise and disorder. *Phys. Rev. Res.* **2**, 033311, DOI: [10.1103/PhysRevResearch.2.033311](https://doi.org/10.1103/PhysRevResearch.2.033311) (2020).
34. Breuer, H.-P. & Petruccione, F. *The Theory of Open Quantum Systems* (Oxford University Press, Oxford, 2007).
35. Weiss, U. *Quantum Dissipative Systems*, 4th ed. (World Scientific, Singapore, 2012).
36. Breuer, H.-P., Laine, E.-M., Piilo, J. & Vacchini, B. *Colloquium*: Non-Markovian dynamics in open quantum systems. *Rev. Mod. Phys.* **88**, 021002, DOI: [10.1103/RevModPhys.88.021002](https://doi.org/10.1103/RevModPhys.88.021002) (2016).
37. de Vega, I. & Alonso, D. Dynamics of non-Markovian open quantum systems. *Rev. Mod. Phys.* **89**, 015001, DOI: [10.1103/RevModPhys.89.015001](https://doi.org/10.1103/RevModPhys.89.015001) (2017).
38. Kennedy, T. A., Colton, J. S., Butler, J. E., Linares, R. C. & Doering, P. J. Long coherence times at 300 K for nitrogen-vacancy center spins in diamond grown by chemical vapor deposition. *Appl. Phys. Lett.* **83**, 4190, DOI: [10.1063/1.1626791](https://doi.org/10.1063/1.1626791) (2003).
39. Herbschleb, E. D. et al. Ultra-long coherence times amongst room-temperature solid-state spins. *Nat. Commun.* **10**, 3766, DOI: [10.1038/s41467-019-11776-8](https://doi.org/10.1038/s41467-019-11776-8) (2019).
40. Balasubramanian, G. et al. Ultralong spin coherence time in isotopically engineered diamond. *Nat. Mater.* **8**, 383, DOI: [10.1038/nmat2420](https://doi.org/10.1038/nmat2420) (2009).
41. Ishikawa, T. et al. Optical and spin coherence properties of nitrogen-vacancy centers placed in a 100 nm thick isotopically purified diamond layer. *Nano Lett.* **12**, 2083–2087, DOI: [10.1021/nl300350r](https://doi.org/10.1021/nl300350r) (2012).
42. Maurer, P. C. et al. Room-temperature quantum bit memory exceeding one second. *Science* **336**, 1283, DOI: [10.1126/science.1220513](https://doi.org/10.1126/science.1220513) (2012).
43. Dutt, M. V. G. et al. Quantum register based on individual electronic and nuclear spin qubits in diamond. *Science* **316**, 1312, DOI: [10.1126/science.1139831](https://doi.org/10.1126/science.1139831) (2007).
44. Zagoskin, A. M., Johansson, J. R., Ashhab, S. & Nori, F. Quantum information processing using frequency control of impurity spins in diamond. *Phys. Rev. B* **76**, 014122, DOI: [10.1103/PhysRevB.76.014122](https://doi.org/10.1103/PhysRevB.76.014122) (2007).
45. Ladd, T. D. et al. Quantum computers. *Nature* **464**, 45, DOI: [10.1038/nature08812](https://doi.org/10.1038/nature08812) (2010).
46. Buluta, I., Ashhab, S. & Nori, F. Natural and artificial atoms for quantum computation. *Rep. Prog. Phys.* **74**, 104401, DOI: [10.1088/0034-4885/74/10/104401](https://doi.org/10.1088/0034-4885/74/10/104401) (2011).
47. Nakazato, T. et al. Quantum error correction of spin quantum memories in diamond under a zero magnetic field. *Commun. Phys.* **5**, 102, DOI: [10.1038/s42005-022-00875-6](https://doi.org/10.1038/s42005-022-00875-6) (2022).
48. Schmitt, S. et al. Submillihertz magnetic spectroscopy performed with a nanoscale quantum sensor. *Science* **356**, 832–837, DOI: [10.1126/science.aam5532](https://doi.org/10.1126/science.aam5532) (2017).

49. Casola, F., van der Sar, T. & Yacoby, A. Probing condensed matter physics with magnetometry based on nitrogen-vacancy centres in diamond. *Nat. Rev. Mater.* **3**, 17088, DOI: [10.1038/natrevmats.2017.88](https://doi.org/10.1038/natrevmats.2017.88) (2018).
50. Dolde, F. et al. Electric-field sensing using single diamond spins. *Nat. Phys.* **7**, 459, DOI: [10.1038/nphys1969](https://doi.org/10.1038/nphys1969) (2011).
51. Dolde, F. et al. Nanoscale detection of a single fundamental charge in ambient conditions using the NV<sup>-</sup> center in diamond. *Phys. Rev. Lett.* **112**, 097603, DOI: [10.1103/PhysRevLett.112.097603](https://doi.org/10.1103/PhysRevLett.112.097603) (2014).
52. McGuinness, L. P. et al. Quantum measurement and orientation tracking of fluorescent nanodiamonds inside living cells. *Nat. Nanotechnol.* **6**, 358, DOI: [10.1038/mnano.2011.64](https://doi.org/10.1038/mnano.2011.64) (2011).
53. Petrini, G. et al. Is a quantum biosensing revolution approaching? perspectives in NV-assisted current and thermal biosensing in living cells. *Adv. Quantum Technol.* **3**, 2000066 (2020).
54. Li, P.-B., Xiang, Z.-L., Rabl, P. & Nori, F. Hybrid quantum device with nitrogen-vacancy centers in diamond coupled to carbon nanotubes. *Phys. Rev. Lett.* **117**, 015502, DOI: [10.1103/PhysRevLett.117.015502](https://doi.org/10.1103/PhysRevLett.117.015502) (2016).
55. Li, P.-B. & Nori, F. Hybrid quantum system with nitrogen-vacancy centers in diamond coupled to surface-phonon polaritons in piezomagnetic superlattices. *Phys. Rev. Appl.* **10**, 024011, DOI: [10.1103/PhysRevApplied.10.024011](https://doi.org/10.1103/PhysRevApplied.10.024011) (2018).
56. Ai, Q. et al. The NV metamaterial: Tunable quantum hyperbolic metamaterial using nitrogen vacancy centers in diamond. *Phys. Rev. B* **104**, 014109, DOI: [10.1103/PhysRevB.104.014109](https://doi.org/10.1103/PhysRevB.104.014109) (2021).
57. Lu, Y.-N. et al. Observing information backflow from controllable non-Markovian multichannels in diamond. *Phys. Rev. Lett.* **124**, 210502, DOI: [10.1103/PhysRevLett.124.210502](https://doi.org/10.1103/PhysRevLett.124.210502) (2020).
58. Takahashi, S., Hanson, R., van Tol, J., Sherwin, M. S. & Awschalom, D. D. Quenching spin decoherence in diamond through spin bath polarization. *Phys. Rev. Lett.* **101**, 047601, DOI: [10.1103/PhysRevLett.101.047601](https://doi.org/10.1103/PhysRevLett.101.047601) (2008).
59. London, P. et al. Detecting and polarizing nuclear spins with double resonance on a single electron spin. *Phys. Rev. Lett.* **111**, 067601, DOI: [10.1103/PhysRevLett.111.067601](https://doi.org/10.1103/PhysRevLett.111.067601) (2013).
60. Palenberg, M. A., Silbey, R. J., Warns, C. & Reineker, P. Local and nonlocal approximation for a simple quantum system. *J. Chem. Phys.* **114**, 4386–4389, DOI: <http://dx.doi.org/10.1063/1.1330213> (2001).
61. Chen, H.-B., Lambert, N., Cheng, Y.-C., Chen, Y.-N. & Nori, F. Using non-Markovian measures to evaluate quantum master equations for photosynthesis. *Sci. Rep.* **5**, 12753, DOI: [10.1038/srep12753](https://doi.org/10.1038/srep12753) (2015).
62. Chruściński, D. & Pascazio, S. A brief history of the GKLS equation. *Open Syst. Info. Dyn.* **24**, 1740001, DOI: [10.1142/S1230161217400017](https://doi.org/10.1142/S1230161217400017) (2017).
63. Redman, D. A., Brown, S., Sands, R. H. & Rand, S. C. Spin dynamics and electronic states of N-V centers in diamond by epr and four-wave-mixing spectroscopy. *Phys. Rev. Lett.* **67**, 3420–3423, DOI: [10.1103/PhysRevLett.67.3420](https://doi.org/10.1103/PhysRevLett.67.3420) (1991).
64. Neumann, P. et al. Multipartite entanglement among single spins in diamond. *Science* **320**, 1326–1329, DOI: [10.1126/science.1157233](https://doi.org/10.1126/science.1157233) (2008).

65. Childress, L. et al. Coherent dynamics of coupled electron and nuclear spin qubits in diamond. Science **314**, 281, DOI: [10.1126/science.1131871](https://doi.org/10.1126/science.1131871) (2006).
66. Liu, G.-Q., Pan, X.-Y., Jiang, Z.-F., Zhao, N. & Liu, R.-B. Controllable effects of quantum fluctuations on spin free-induction decay at room temperature. Sci. Rep. **2**, 432, DOI: [10.1038/srep00432](https://doi.org/10.1038/srep00432) (2012).
67. Maze, J. R. et al. Free induction decay of single spins in diamond. New J. Phys. **14**, 103041, DOI: [10.1088/1367-2630/14/10/103041](https://doi.org/10.1088/1367-2630/14/10/103041) (2012).
68. Jacques, V. et al. Dynamic polarization of single nuclear spins by optical pumping of nitrogen-vacancy color centers in diamond at room temperature. Phys. Rev. Lett. **102**, 057403, DOI: [10.1103/PhysRevLett.102.057403](https://doi.org/10.1103/PhysRevLett.102.057403) (2009).
69. Fischer, R. et al. Bulk nuclear polarization enhanced at room temperature by optical pumping. Phys. Rev. Lett. **111**, 057601, DOI: [10.1103/PhysRevLett.111.057601](https://doi.org/10.1103/PhysRevLett.111.057601) (2013).
70. Álvarez, G. A. et al. Local and bulk  $^{13}\text{C}$  hyperpolarization in nitrogen-vacancy-centred diamonds at variable fields and orientations. Nat. Commun. **6**, 8456, DOI: [10.1038/ncomms9456](https://doi.org/10.1038/ncomms9456) (2015).
71. King, J. P. et al. Room-temperature in situ nuclear spin hyperpolarization from optically pumped nitrogen vacancy centres in diamond. Nat. Commun. **6**, 8965, DOI: [10.1038/ncomms9965](https://doi.org/10.1038/ncomms9965) (2015).
72. Scheuer, J. et al. Optically induced dynamic nuclear spin polarisation in diamond. New J. Phys. **18**, 013040, DOI: [10.1088/1367-2630/18/1/013040](https://doi.org/10.1088/1367-2630/18/1/013040) (2016).
73. Chakraborty, T., Zhang, J. & Suter, D. Polarizing the electronic and nuclear spin of the NV-center in diamond in arbitrary magnetic fields: analysis of the optical pumping process. New J. Phys. **19**, 073030, DOI: [10.1088/1367-2630/aa7727](https://doi.org/10.1088/1367-2630/aa7727) (2017).
74. Scheuer, J. et al. Robust techniques for polarization and detection of nuclear spin ensembles. Phys. Rev. B **96**, 174436, DOI: [10.1103/PhysRevB.96.174436](https://doi.org/10.1103/PhysRevB.96.174436) (2017).
75. Hovav, Y., Naydenov, B., Jelezko, F. & Bar-Gill, N. Low-field nuclear polarization using nitrogen vacancy centers in diamonds. Phys. Rev. Lett. **120**, 060405, DOI: [10.1103/PhysRevLett.120.060405](https://doi.org/10.1103/PhysRevLett.120.060405) (2018).
76. Henshaw, J. et al. Carbon-13 dynamic nuclear polarization in diamond via a microwave-free integrated cross effect. Proc. Natl. Acad. Sci. U.S.A. **116**, 18334, DOI: [10.1073/pnas.1908780116](https://doi.org/10.1073/pnas.1908780116) (2019).